

PL-TR-97-2127

## RESEARCH ON SEISMIC MONITORING AT REGIONAL DISTANCES

M. Imhof  
B. Nolte  
W. Rodi  
M. N. Toksöz

Earth Resources Laboratory  
Department of Earth, Atmospheric, and  
Planetary Sciences  
Massachusetts Institute of Technology  
Cambridge, Massachusetts 02139

10 September 1997

Final Report  
30 June 1995-30 June 1997

**19980413 035**

APPROVED FOR PUBLIC RELEASE; DISTRIBUTION UNLIMITED



**PHILLIPS LABORATORY**  
Directorate of Geophysics  
AIR FORCE MATERIEL COMMAND  
HANSCOM AIR FORCE BASE, MA 01731-3010

[**DIGITAL QUALITY ELECTROSTATIC 6**]

SPONSORED BY  
Air Force Technical Applications Center  
Directorate of Nuclear Treaty Monitoring  
Project Authorization T/5101

MONITORED BY  
Phillips Laboratory  
CONTRACT No. F19628-95-C-0091

The views and conclusions contained in this document are those of the authors and should not be interpreted as representing the official policies, either express or implied, of the Air Force or U.S. Government.

This technical report has been reviewed and is approved for publication.



JAMES C. BATTIS  
Contract Manager



CHARLES P. PIKE, Director  
Business Management Division

This report has been reviewed by the ESD Public Affairs Office (PA) and is releasable to the National Technical Information Service (NTIS).

Qualified requestors may obtain copies from the Defense Technical Information Center. All others should apply to the National Technical Information Service.

If your address has changed, or you wish to be removed from the mailing list, or if the addressee is no longer employed by your organization, please notify PL/IM, 29 Randolph Road, Hanscom AFB, MA 01731-3010. This will assist us in maintaining a current mailing list.

Do not return copies of the report unless contractual obligations or notices on a specific document requires that it be returned.

# REPORT DOCUMENTATION PAGE

Form Approved  
OMB No. 0704-0188

Public reporting burden for this collection of information is estimated to average 1 hour per response, including the time for reviewing instructions, searching existing data sources, gathering and maintaining the data needed, and completing and reviewing the collection of information. Send comments regarding this burden estimate or any other aspect of this collection of information, including suggestions for reducing this burden, to Washington Headquarters Services, Directorate for Information Operations and Reports, 1215 Jefferson Davis Highway, Suite 1204, Arlington, VA 22202-4302, and to the Office of Management and Budget, Paperwork Reduction Project (0704-0188), Washington, DC 20503.

<b>1. AGENCY USE ONLY (Leave blank)</b>			<b>2. REPORT DATE</b> 10 September 1997		<b>3. REPORT TYPE AND DATES COVERED</b> Final (6/30/95-6/30/97)		
<b>4. TITLE AND SUBTITLE</b>  Research on Seismic Monitoring at Regional Distances			<b>5. FUNDING NUMBERS</b>  F19628-95-C-0091  PE 5999F PR 5101 TA GM WU AI				
<b>6. AUTHOR(S)</b>  Matthias Imhof                            William Rodi Bertram Nolte                            M. Nafi Toksöz			<b>7. PERFORMING ORGANIZATION NAME(S) AND ADDRESS(ES)</b>  Earth Resources Laboratory Dept. of Earth, Atmospheric, & Planetary Sciences Massachusetts Institute of Technology 42 Carleton Street Cambridge, MA 02142				
<b>9. SPONSORING/MONITORING AGENCY NAME(S) AND ADDRESS(ES)</b>  Phillips Laboratory Geophysics Directorate 29 Randolph Road Hanscom AFB, MA 01731-3010 Contract Manager: Mr. James Battis/GPE			<b>8. PERFORMING ORGANIZATION REPORT NUMBER</b>  63575				
<b>11. SUPPLEMENTARY NOTES</b>			<b>10. SPONSORING/MONITORING AGENCY REPORT NUMBER</b>  PL-TR-97-2127				
<b>12a. DISTRIBUTION / AVAILABILITY STATEMENT</b>  Approved for Public Release: Distribution Unlimited			<b>12b. DISTRIBUTION CODE</b>				
<b>13. ABSTRACT (Maximum 200 words)</b>  We report two studies related to numerical modeling of seismic wave generation and propagation. In the first, we use a 2-D multiple multipole method to model seismic wave radiation from nuclear explosions in and near underground cavities. Our modeling results are used to interpret seismograms recorded during the Non-Proliferation Experiment (NPE), which occurred near a large complex of tunnels and cavities. Synthetic seismograms for a simplified NPE geometry correlate well with the observed S-wave energy generated at or near the source and, by including near-receiver tunnels into our models, we obtain the observed coupling between the radial and transverse component.  The second study demonstrates the advantages of a newly developed irregular-grid modeling technique for seismic wave propagation in laterally varying media. A numerical example demonstrates that the technique is more accurate than a standard regular-grid finite-difference method for modeling the effects of irregular interfaces. We then show that the method can be applied to models with irregular free-surface topography, suggesting that our new variable-grid method may be a valuable alternative to existing finite-difference free-surface algorithms. We demonstrate the effect of irregular surface topography on regional wave propagation with a Middle East example.						<b>14. SUBJECT TERMS</b>  Explosions in cavities, irregular-grid finite difference, regional wave propagation, elastic wave modeling, Non-Proliferation Experiment (NPE)	
<b>17. SECURITY CLASSIFICATION OF REPORT</b> UNCLASSIFIED			<b>18. SECURITY CLASSIFICATION OF THIS PAGE</b> UNCLASSIFIED		<b>19. SECURITY CLASSIFICATION OF ABSTRACT</b> UNCLASSIFIED		
<b>20. LIMITATION OF ABSTRACT</b> SAR			<b>15. NUMBER OF PAGES</b> 88				
			<b>16. PRICE CODE</b>				

## TABLE OF CONTENTS

List of Contributing Scientists .....	v
List of Previous and Related Contracts .....	v
Bibliography of Publications Totally or Partially Supported by the Contract .....	v
Preface .....	vii
Calculating Seismic Radiation Patterns for Explosions in and Around Cavities ....	1
Abstract .....	1
Introduction .....	2
Effect of Cavities Near the Source .....	5
Effect of a Row of Cavities .....	7
Effects of Cavity Shapes and Source Types .....	8
Application to the Non-Proliferation Experiment .....	12
Summary .....	16
Acknowledgments .....	17
Appendix A: Elastic Multiple Multipole Expansions .....	17
Appendix B: Moment Tensor from Multiple Multipole Expansions .....	19
References .....	23
Table .....	28
Figures .....	29
Simulation of Elastic Wave Propagation in Models Containing Irregular Interfaces Parameterized in Irregular Grids .....	47
Abstract .....	47
Introduction .....	48
The Modeling Technique .....	49
Comparison With Finite Difference for a Dipping Interface .....	50
A Simple Free-Surface Example .....	52
Modeling Rough-Topography Effects on Regional Wave Propagation .....	53
Discussion .....	54

Conclusions .....	55
References .....	56
Appendix .....	59
Figures .....	62

## List of Contributing Scientists

Matthias Imhof, Postdoctoral Fellow, Massachusetts Institute of Technology  
Bertram Nolte, Research Scientist, Massachusetts Institute of Technology  
William Rodi, Research Scientist, Massachusetts Institute of Technology  
M. Nafi Toksöz, Professor of Geophysics, Massachusetts Institute of Technology

## List of Previous and Related Contracts

DARPA/AFGL Contract F19628-89-K-0020, "Regional Seismograms: Attenuation and Scattering", July 1989-June 1991.

DARPA/AFPL Contract F19628-90-K-0057, "Research in Regional Seismology: The Effect of Anisotropy", August 1990 to July 1992.

DARPA/AFPL Contract F29601-91-K-DB15, "Research on Monitoring at Regional Distances", September 1991 to September 1993.

AFOSR Contract F49620-92-J-0413, "Basic Research in Nuclear Test Monitoring", July 1992 to July 1994.

AFOSR Contract F49620-93-1-0424, "Seismic Wave Radiation, Propagation and Event Location in Laterally Heterogeneous Media", July 1993 to December 1994.

AFOSR Grant F49620-94-1-0282, "Effect of 3D Heterogeneities and Topography on Seismic Wave Propagation and the Use of Empirical Green's Functions for Source Characterization and Discrimination", May 1994 to May 1996.

AFOSR Grant F49620-94-1-0273, "Characterization of Seismic Sources Using Empirical Green's Functions", July 1994 to June 1997.

DARPA/AFPL Contract F19628-95-K-0008, "Application of Parallel Computing Algorithms to Three-Dimensional Modeling of Seismic Waves Generated by Complex Sources in Inhomogeneous Media", July 1995 to March 1997.

## Bibliography of Publications Totally or Partially Sponsored by the Contract

R.L. Gibson, Jr., M.N. Toksöz, and W. Dong, "Seismic sources and wave propagation in 3D: radiation from cylindrical cavities", *Proc. 17th Ann. Seismic Research Symp.*, Scottsdale, AZ, Air Force Phillips Laboratory, 1995.

R.L. Gibson, Jr., M.N. Toksöz, and W. Dong, "Seismic radiation from explosively loaded cavities in isotropic and transversely isotropic media", *Bull. Seism. Soc. Am.*, 86, 1910-1924, 1996.

B. Nolte, R.L. Gibson, Jr., and M.N. Toksöz, "Irregular-grid modeling of regional wave propagation", *Proc. 18th Ann. Seismic Research Symp.*, Annapolis, MD, Air Force Phillips

Laboratory, 1996.

M.G. Imhof and M.N. Toksöz, "Seismo-acoustic multiple scattering: a comparison of multiple multipole expansions with an ultrasonic experiment", *J. Acoust. Soc. Am.*, 101, 1836-1846, 1997.

M.G. Imhof and M.N. Toksöz, "Calculating seismic source signatures for explosions in and around cavities", submitted to *19th Research Symp. on Monitoring a Comprehensive Test Ban Treaty*, Orlando, FL, Defense Special Weapons Agency, 1997.

M.G. Imhof and M.N. Toksöz, "Calculating seismic source signatures for explosions in and around cavities", submitted to *Bull. Seism. Soc. Am.*, 1997.

## PREFACE

The work we report here has two primary objectives; (1) to investigate the effects of near-source heterogeneity on the radiation from explosion sources, and (2) to develop improved methods for modeling regional wave propagation in laterally varying media.

The first section of this report is a preprint of an article submitted to *Bulletin of the Seismological Society of America* and deals with nuclear explosions in and near underground cavities. Using numerical modeling with a 2-D multiple multipole method, we study the source radiation from an explosion in a cavity including the effects of scattering from a nearby cavity. We also study the radiation from an explosion in a regular arrangement of cavities and in a particular ‘L’-shaped cavity geometry representing a large tunnel with a side-drift. Our modeling results are used to interpret seismograms recorded during the Non-Proliferation Experiment (NPE), which showed strong azimuthal variation in waveforms and amplitudes that can be explained only partially by heterogeneities along the path of propagation or near the receiver. Near the NPE source there was a large complex of tunnels and cavities. Synthetic seismograms for a simplified NPE geometry correlate nicely with the observed S wave energy generated at or near the source. By including near-receiver tunnels into our model, we also obtain the observed coupling between the radial and transverse component.

The second section of this report describes a new technique we have developed for computing synthetic seismograms in laterally varying media. This technique parameterizes the

model on a (possibly irregular) triangular grid and uses a discrete approximation to the integral form of the wave equation. An irregular grid has the advantage that it can be aligned with irregular interfaces present in a model, in particular an irregular free surface. The method is thus useful for the incorporation of surface topography into a model, which is essential for the modeling of regional wave propagation in many important geographic areas, e.g. the Middle East. Another attractive feature of irregular-grid modeling is the possibility of locally adapting the grid spacing to the wave speed, saving memory and computer time. We first demonstrate the improved accuracy of the method for irregular interfaces through a comparison with finite differences. We then present two models that show the effect of a rough surface topography on regional seismograms.

# **Calculating Seismic Radiation Patterns for Explosions in and Around Cavities**

## **Abstract**

Seismic sources can be located in an underground complex of tunnels and cavities. Examples of such sources are chemical or nuclear devices as well as mining-related events. Cavities are very strong scatterers which affect radiation patterns and conversions between different wavetypes.

We use a 2-D multiple multipole method to calculate source radiation patterns and scattering from cavities. We illustrate the effects of distance between source cavity and a scatterer, the effect of a regular arrangement of cavities and the location of the source therein, and the effect of different source mechanisms for a particular 'L'-shaped geometry representing a large tunnel with a source in a side-drift.

Seismograms recorded during the Non-Proliferation Experiment (NPE) show strong azimuthal variations in waveforms and amplitudes which can be explained only partially by heterogeneities along the path of propagation or near the receiver. Near the NPE source, there was a large complex of tunnels and cavities. Synthetic seismograms for a simplified NPE geometry correlate nicely with

data observed around the arrival of S-waves generated at or near the source. By including near-receiver tunnels into our model, we also obtain the observed coupling between the radial and transverse component.

## Introduction

Discrimination between seismic sources such as earthquakes, quarry or mine blasts, and nuclear explosions becomes increasingly difficult as the magnitude of the events decreases (Blandford, 1981; Li *et al.*, 1996). The ability to extract useful information about seismic sources from seismic waveform data is limited by the complexity of the seismograms and the ability to model these complexities. For example, spall, tectonic release processes, and scattering contribute strongly to far-field seismic wave signals. The classic explosion source model, which yields an isotropic P-wave radiation pattern, cannot reproduce observed waveforms.

Signal-generated “noise” is particularly treacherous in this respect, as it typically has the transient character and frequency content which can easily be misinterpreted as due to some property of the source. For example, changes in source cavity shape and source location within the cavity influence the radiation pattern of the explosion by decoupling (Latter *et al.*, 1961). Although many studies have been made, numerical (e.g., Gibson *et al.*, 1996) and analytical results (e.g., Ben-Menahem and Mikhailov, 1995) apply different assumptions and produce different results. Zhao and Harkrider (1992) developed solutions for the displacement field created by an explosion source located off-center within a solid sphere embedded in an infinite solid medium, a model of a fully tamped explosion. Here the loss of symmetry causes shear waves to be generated, even with the

spherical cavity. Other studies have examined the effect of varying the cavity shape. Rial and Moran (1986), Glenn and Rial (1987), and Gibson *et al.* (1996) considered ellipsoidal and cylindrical cavity shapes, and, applying a combination of numerical and approximate analytical methods, obtained estimates of far-field radiation patterns. They suggested that the P-wave radiation would be strongest perpendicular to an ellipsoidal cavity and that a fairly strong S-wave would be generated as the cavity aspect ratio (ratio of length to diameter) became large. Stevens *et al.* (1991) and Murphy *et al.* (1995) also examined an ellipsoidal cavity. However, in contrast with the earlier results, they concluded that at the frequencies of interest for regional wave propagation, the P-wave radiation pattern would be fairly isotropic and S-wave amplitudes comparatively small.

In the above studies, the effect of other heterogeneities has been mostly ignored. However, App *et al.* (1995) found that a horizontal discontinuity near an explosion source generated enough S-waves to influence regional waveforms, and thus cause such an explosion to appear more earthquake-like. For explosions at the Nevada Test Site, Stump *et al.* (1994) noted that at very closed-in distances, the transverse component of motion contained a source signature which relates to some type of scattering mechanism. An analysis of seismic data from the Non-Proliferation Experiment (NPE) showed that elastic wave scattering near the receiver had a significant effect upon the recorded waveforms (Johnson, 1995). Kamm and Bos (1995) calculated the effects of the layered structure on the NPE to study the scattering along the path of propagation. Their results indicate that the velocity structure alone cannot explain the scattered waves.

Chemical or nuclear devices are commonly exploded within underground complexes with various explosion chambers as well as shafts and tunnels used for access and instrumentation (Denny and

Stull, 1994). Moreover, there exist other seismic sources which occur in or near underground complexes such as mines: e.g. rockbursts (Bennett *et al.*, 1995), collapses (Pearson *et al.*, 1996), or mining related explosions (Reamer *et al.*, 1992). But cavities are extremely strong scatterers which efficiently convert different wave-types into each other. The scatterers act as secondary sources with different radiation patterns and different distance dependencies than the primary waves. The discrimination between different seismic sources is made much more difficult by these secondary signals.

The objective of this paper is to study how the shape of the source cavity and the scattering by heterogeneities in the near-field of the source, such as tunnels and other cavities, affect the radiation of seismic waves. Characterizing seismic radiation from such complex source geometries requires an accurate and efficient computational method that will work for complex arrangements of cavities with a source in any part of a cavity complex. For this purpose, we developed the 2-D Multiple MultiPole (MMP) method (Imhof, 1996). In the MMP method, scattered wavefields are expanded into a set of basis functions which are solutions to the wave equation in a homogeneous medium. To find the yet unknown weighting coefficient for each basis function, we choose discrete matching points along the boundaries of the scatterers where we satisfy the boundary conditions. Each matching point provides two equations corresponding to vanishing tractions which build a linear matrix system for the unknown weighting coefficients. Typically, the chosen basis functions are scalar Helmholtz potentials of multipole form for P- and S-waves. In contrast to more traditional methods, we use multiple expansion centers and thus multiple multipoles for each scatterer. However, these basis functions are not orthogonal, leading us to overdetermine the linear matrix

system and solve it in the least-squares sense. The method has been described in detail in a previous publication (Imhof, 1996), and in Appendix A we outline the method as necessary for the present work. For a more complete discussion on usage and implementation, the reader is referred to the previous paper. For some models, we will convert the MMP solutions into moment tensor expansions. The relation between the MMP expansion and the moment tensor is presented in Appendix B.

The paper is structured as follows. First, we illustrate the effect of distance between an axially symmetric source-cavity and a scatterer. We also show how a regular arrangement of cavities affects the radiation patterns as a function of source location. Second, we exemplify the effect of asymmetric cavity shapes. A small source cavity is placed near a large tunnel. We show the radiation patterns for only the source cavity, the tunnel in the near-field of an isotropic explosion source, and combined models with different source mechanisms. Finally, we apply our findings to the Non-Proliferation Experiment. We interpret phases recorded around the arrival time of S-waves by near-source scattering and explain the coupling between radial and transverse component by near-receiver heterogeneities.

## Effect of Cavities Near the Source

As a first example, we calculate how a 2-D cylindrical scatterer in the near-field of the source affects the radiated waves. This simple example serves two purposes: First, as a check for the numerical method we use. Second, the example shows that a scatterer in the near-field of the source has a pronounced effect on the source signature. A schematic of the example is shown in Figure 1.

Two cylindrical cavities with a radius of 7.5 m are embedded in a homogeneous fullspace with density  $\rho = 1800 \text{ kg/m}^3$ , P-wave velocity  $v_p = 2000 \text{ m/s}$ , and S-wave velocity  $v_s = 1110 \text{ m/s}$ . One cavity (source) is assumed to be instantaneously pressurized by an explosion (Patton, 1991). The center-frequency of the radiated wave is 10 Hz.

Radiation patterns  $R(\phi)$  as a function of azimuth  $\phi$  are calculated for radial and transverse polarizations:

$$R_i(\phi) = \int_0^\infty (\dot{u}_i(r_0, \phi, \tau))^2 d\tau, \quad (1)$$

where the subscript  $i$  denotes radial or transverse component of the total displacement  $\mathbf{u}(\mathbf{x}, t)$  at location  $\mathbf{x} = (r_0, \phi)$ . The distance  $r_0$  is 750 m. We do not need to decompose the seismograms into P- and S-waves. Although the P-waves (S-waves) will bleed into the transverse (radial) component, the radial (transverse) radiation pattern is dominated by the P-waves (S-waves).

Due to the circular cross-section in this 2-D example, the source emits only P-waves where the amplitudes are independent of angle. However, the second cavity placed nearby perturbs the isotropic P-wave radiation pattern and acts as a secondary S-wave source (Figure 2). The farther the two cavities are separated, the smaller the effect of the scatterer becomes. Although the P-wave radiation pattern is clearly anisotropic for small separations (20 m), it is the S-wave radiation pattern which is affected the most. While the S-wave displacement is nearly comparable to the P-wave displacement at 20 m, it vanishes quickly with increasing separation. But as the overlay of the results from all cavity locations shows, the originally isotropic P-wave radiation patterns is only slightly perturbed by the presence of additional cavities in the near-field of the source.

The rapid decay of the S-wave conversion is presented in Figure 3. Shown is the ratio between

the maximal S-wave radiation and the isotropic P-wave radiation as a function of separation between the two cavities. While the ratio is as high as 0.7 for a distance of 20 m, it decays rapidly until it reaches a nearly constant value of 0.07 for distances of 300 m and more. Hence for multiple cavities, we expect only cavities within a dominant shear wavelength (110 m) from the source to influence the S-wave conversion and thus the S-wave radiation pattern. The effects from cavities at larger distances will be overshadowed by cavities near-source and near-receiver heterogeneities.

### Effect of a Row of Cavities

Although we concluded from the previous numerical experiment that the effect of other cavities vanishes rapidly with increasing distance, there still are interesting effects to be observed. The geometry of a complex of cavities, drifts, and shafts might not be random but systematic and orderly. A likely arrangement of explosion chambers would be an array of evenly spaced cavities. The configuration we look at is an array of cavities with a radius of 7.5 m and a spacing of 50 m. Assuming an array of 9 cavities, we will pressurize each of them in a sequence (Figure 4). For each source, we will calculate the overall radiation pattern as a function of position in the sequence. The model parameters are the same as in the previous one: 2-D model, density  $\rho = 1800 \text{ kg/m}^3$ , P-wave velocity  $v_p = 2000 \text{ m/s}$ , S-wave velocity  $v_s = 1110 \text{ m/s}$ , and center-frequency 10 Hz.

Figure 5 presents the radiation patterns for the source chambers 1, 3, and 5. The first explosion is the most asymmetric configuration, while the fifth explosion will be in a symmetrical one. Although the P-wave radiation pattern is anisotropic for each case, the overlay of the three cases shows that the P-wave pattern hardly depends on the choice of the source chamber within the array. Clearly, the S-wave pattern exhibits more change. While the pattern itself changes only slightly, the

amplitudes in the forward direction exhibit the greatest effect. In this direction, the conversion to S-waves doubles between source chamber 1 and 5. For source chamber 5, the ratio of S-wave radiation to P-wave radiation reaches as high as 0.6. The efficiency of the P to S conversion as a function of source chamber is shown in Figure 6. Once the source chamber is within the array, the ratio of S-wave radiation to P-wave radiation stays close to 0.6 for all source chambers. The exceptions are the first and the last source chamber, each of which has only one neighboring cavity. However, even for these extremal geometries, the conversion to S-waves is much stronger than expected for a separation of 50 m between source chamber and an adjacent cavity. Comparison of Figures 3 and 6 shows that the ratio is two to three times higher than expected for this separation distance. Thus, in the array configuration, cavities at larger distances still contribute to the conversion due to multiple scattering between the cavities.

## Effects of Cavity Shapes and Source Types

The two examples in the previous section were both for axially symmetric cavities. Here, we will address the effect of asymmetrical cavities. The 2-D geometry we will use is shown in Figure 7. The situations we study are sketched in Figure 8. The models consist of (a) a source in a small, elongated cavity ( $26 \times 10$  m), (b) an explosive line source near a large cavity ( $60 \times 18$  m), and (c) both cavities together representing a large access tunnel with a source in a perpendicular side drift. The distance between the two cavities is 10 m. The geometry is not plane-symmetric. The small source cavity is offset by 15 m from the center of the larger one. At a distance of 750 m, we calculate the radiation patterns. As the source cavity is not axially symmetric, it will radiate both P- and

S-waves. The model parameters are: density  $\rho = 1800 \text{ kg/m}^3$ , P-wave velocity  $v_p = 2000 \text{ m/s}$ , S-wave velocity  $v_s = 1110 \text{ m/s}$ , and center-frequency 10 Hz.

The first numerical experiment is simply to determine the radiation pattern for the source cavity only. Thus, we omit the large cavity for this calculation. As a source, we choose an instantaneous pressurization of the cavity. Figure 8(a) shows a sketch of the model and the resulting radiation patterns of P- and S-waves. The ratio between peak amplitudes of P- and S-waves is very close to unity. As expected, we obtain a large S-wave component with a radiation pattern typical for a double-coupled system of forces. For the P-waves, we see a combination of isotropic radiation (point source) and quadrupole radiation (double-coupled force system). Both in our calculation and those of Rial and Moran (1986), Glenn and Rial (1987), or Gibson *et al.* (1996), the P-wave radiation is strongest perpendicular to the elongated cavity-axis. In contrast to these results, Stevens *et al.* (1991) and Murphy *et al.* (1995) stated that at the frequencies of interest for regional wave propagation, the P-wave radiation patterns would be fairly isotropic and the S-wave amplitudes would be comparably small based on their finite-stress amplitude calculations. For small sources placed in cavities, elastic behavior would be a valid approximation, and our results should represent the radiation patterns.

As a next step, we determine the effects of the large access tunnel. We replace the source cavity with an isotropic, explosive line source located at the center of gravity of the source cavity. With this arrangement, there is no interaction between the scatterer and the source. A schematic of the model and the resulting radiation patterns are shown in Figure 8(b). The P-wave radiation is strongly affected by the tunnel. The tunnel effectively blocks the propagation of P-waves. The

radiation pattern exhibits some degree of symmetry. However, the patterns are not aligned with the scatterer due to the asymmetrical configuration of source and scatterer.

The S-wave radiation pattern still resembles a deformed double-couple. Interestingly, the ratio of S- to P-waves remains very close to unity. These two examples clearly show that both the geometry of the source cavity as well as additional cavities in the near-field of the source generate similar effects, i.e. conversion of P- to S-waves and angularly asymmetric radiation patterns.

We now calculate the combined model where we have an instantaneously pressurized source chamber with a large scatterer nearby. Thus, the source chamber radiates P- and S-waves as shown in Figure 8(a). However, these fields interact now with the large access tunnel. We expect the symmetry in the radiation patterns to diminish which is exactly what happens. Figure 8(c) shows the resulting radiation patterns for the combined model. The P-wave radiation pattern still resembles the original pattern as radiated from the source, although there is less P-wave radiation. Also, the symmetry of the radiation pattern is broken. The big difference lies in the S-wave radiation. The S-wave radiation is enhanced by a factor of at least 1.5. There is a significant increase in S-wave radiation in the diagonal direction. To examine the radiation pattern further, we convert the MMP solution into a moment tensor. The relation between MMP solution and moment tensor is derived in Appendix B. This conversion will allow us to relate our numerical results to observations where the moment tensor is routinely estimated (e.g. Patton, 1991; Johnson and McEvilly, 1994).

The moment tensor expansion describes a complex seismic source as a linear superposition of an explosion source  $p$ , two point forces  $f_1$ ,  $f_2$ , and two double-couple force-systems  $m$ ,  $n$ . All

components are located at the origin. Customarily, higher order source components are neglected. The components can either be represented as a function of frequency or as a function of time. In the latter case, we obtain the source-time-history. However, there also exists a complementary set of components. The first component is the rotational source  $\tilde{s}$  corresponding to a torque. The remaining ones are non-physical forces  $\tilde{f}_1$ ,  $\tilde{f}_2$ , and non-physical double-couples  $\tilde{m}$ ,  $\tilde{n}$ . Their P- and S-wave radiation patterns are aligned instead of interlaced as for physical ones. These patterns violate assumptions underlying linear, elastic wave theory. We choose the Haskell's source-time function with  $B = -0.1$  and  $k = 25.0 \text{ s}^{-1}$  (Haskell, 1967).

The different components of the moment tensor expansion are shown in Figure 10(a). The moment tensor is strongly deviatoric which corresponds to a large contribution of the  $m$  double-couple. Interestingly, the presence of the large scatterer in the near-field of the source induces a torque as indicated by the  $\hat{s}$  component. Numerical experiments showed that moving the scatterer downwards into a more symmetric position diminishes the torque component  $\hat{s}$ . Similarly, moving the scatterer into the far-field or reducing its size decreases its strength. Thus, the presence of the torque term is caused by the asymmetric geometry. Both the isotropic component  $p$  as well as the off-diagonal double-couple  $n$  contribute very little compared to the deviatoric double-couple  $m$ . As expected, the physical point forces  $f_1$ ,  $f_2$  and the non-physical components  $\tilde{f}_1$ ,  $\tilde{f}_2$ ,  $\tilde{m}$ , and  $\tilde{n}$  do not contribute.

An interesting extension of the previous discussion is to change the source mechanism. So far, we only used isotropic explosion sources or instantaneous pressurization of cavities. Neither is a realistic model for underground mining where explosive charges commonly are placed in drill-holes

at the front of drifts. To study the difference, we prescribe tractions only along one front of the source chamber. This source type corresponds to a point force perpendicular to the front. Figure 9 presents a sketch of the model and the resulting radiation patterns. Clearly, the point force is the main contribution for both P- and S-wave radiation. However, the patterns are asymmetric due to interaction of the waves with the large scatterer. These findings are consistent with the moment tensor shown in Figure 10(b) where the largest contribution comes from the point force  $f_1$ . Again, the non-physical terms  $\tilde{f}_1$ ,  $\tilde{f}_2$ ,  $\tilde{m}$ , and  $\tilde{n}$  vanish.

The radiation patterns for the two different source mechanisms ‘instantaneous pressurization’ and ‘frontal explosion’ are clearly very different. The presence of the access tunnel (large scatterer) makes the radiation patterns deviate dramatically from the ideal ones.

## Application to the Non-Proliferation Experiment

On September 22, 1993, the Non-Proliferation Experiment (Denny and Stull, 1994) was conducted at the Nevada Test Site (NTS). A large chemical charge equivalent to 1.1 kt TNT was detonated in a cavity off from the N-Tunnel in Area 12. The purpose of the experiment was to quantify the effects of a chemical explosion of magnitude comparable to that of nuclear explosions. The charge was emplaced in a cylindrical cavity of nominal height of 5.2 m and diameter 15.2 m at a nominal depth of 389 m. The source was embedded in zeolitized tuff with  $v_p = 2400.0$  m/s,  $v_s = 1180.0$  m/s, and  $\rho = 1800.0$  kg/m<sup>3</sup> (Kamm and Bos, 1995). The local stratigraphy was determined from three vertical drill holes in a range of 300 m from the source.

Figure 11 shows seven seismograms recorded at the surface within a range of 558 – 920 m from

the center of the NPE explosion at different azimuths. Range and azimuth are defined in Figure 11 and Table I (Kamm and Bos, 1995). Clearly, the first motions, which correspond to the primary P-wave, are along the radial, upward direction. The remainder of the seismograms is composed of reflections and conversions of the initial wave. Olsen and Peratt (1994) speculated that scattering processes due to medium heterogeneities cause this effect. Johnson (1995) explained these events with scattering from heterogeneities near the receivers. App and Brunish (1991) explained similar variations by reflections from a dipping low velocity layer. Although there is a slight dip present in the local strata (Baldwin *et al.*, 1994), we do not expect azimuthal variations of such a strength. We believe that another possible scattering mechanism – other cavities close to the source – may also have contributed. For obvious reasons, the source cannot be placed in pristine material. The source cavity will necessarily be surrounded by a large, complex network of caverns, drifts, and shafts. These cavities can be of dimensions comparable to the dominant wavelength. Furthermore, some cavities are located within a dominant wavelength from the source. Hence, it is important to recognize these caverns as strong scatterers, acting as secondary sources contributing to the received signals.

We used the 2-D MMP technique (Imhof, 1996) to analyze the effect of the caverns and tunnels. The complicated NPE geometry shown in Denny and Stull (1994) was simplified to the model shown in Figure 12. Due to the 2-D geometry, each cavity extends to infinity along the z-direction. To calculate seismograms, we choose a source-time function as suggested by Haskell (1967) for an underground explosion where  $B = -0.075$  and  $k = 30.0 \text{ s}^{-1}$  which yields a source-time function comparable to that observed by Johnson and McEvilly (1994). Figure 13 shows the synthetic

moment tensor as a function of time. The moment tensor is obtained from the MMP solution by applying the conversion given in Appendix B. The synthetic moment-tensor and the observed one compare well. Both contain only small non-isotropic components.

At a distance of 750 m, we calculate the radial and transverse accelerations as a function of time and azimuth. Figure 14 shows the synthetic seismograms. There is very little bleeding of energy from the radial component to the transverse one and vice versa. This suggests that the radial component contains mainly the P-wave, while the transverse one contains the S-wave. Clearly, for waves propagating toward the east (Figure 12), the pulse broadens due to the reflection off the cavities. In contrast, P-waves propagating westward arrive with a delay caused by the obstruction from the tunnels. For S-waves, we obtain a different picture. S-waves propagating east arrive later due to their increased path from the scattering tunnels. Waves propagating toward the northwest arrive earlier due to their shorter path. Unfortunately, the dependence of amplitude on azimuth is not easily seen on the seismograms.

Figure 15 shows the corresponding radiation patterns as defined in equation (1). The major part of the P-wave energy radiates toward the unobstructed southeast. S-waves appear to propagate predominantly in the northeast and southward directions. Also, there are two lobes which correspond to S-waves generated at the south end of the access drift and in the gaps between the three cavities.

Figure 16 shows a comparison between observed accelerations recorded in the tunnel complex and the synthetics neglecting the effect of near-receiver heterogeneities. The observed accelerations are plotted in [ $\text{m/s}^2$ ]. For the comparison, the observed traces are bandpass filtered to contain a

frequency content similar to the synthetics. As a filter, we use the Fourier transform of a zero-phase Ricker wavelet with the spectrum  $S(f) = (f/f_0)^2 \exp\{-(f/f_0)^2\}$  where  $f_0 = 27$  Hz. All synthetic traces are scaled equally, preserving the true amplitude ratios between the different receivers and components.

For all four stations, synthetics and observations correlate well for early arrivals on the radial component. These arrivals correspond to the initial P-wave and its reflections from heterogeneities along the path of propagation. On the transverse component, observed and synthetic traces correlate well around the arrival of S-waves generated near the source. These events propagated most of their path with S-wave velocities. Not only are the envelopes of the amplitudes comparable, but also their phases. In the synthetics, these S-waves dominate the transverse component.

However, these synthetics do not explain the prominent transverse arrivals at or near the P-wave arrival time. The accelerometers were grouted into small holes near access tunnels which act as near-receiver scatterers. To show their effects, we repeat the calculations but including near-receiver tunnels. As shown in Figure 17, synthetics and observations correlate well for early arrivals on both components for all stations. The applied scaling is the same as in Figure 16. Although these arrivals propagated predominantly as P-waves on the radial component, the near-receiver heterogeneity couples these events to the transverse component and thus to S-waves. Similarly, transverse arrivals are imprinted onto the radial component. In conclusion, both components contain large S-wave contributions caused by near-source scattering. The components are coupled by near-receiver scattering.

## Summary

We have investigated the effects of scattering by cavities near the source or near the receivers. Our numerical analysis showed that scattering in the near-field of the source has a significant effect upon both the observed waveforms and the radiation patterns. In our examples, the ratio between peak amplitudes of P- and S-waves ranges from 10 to 70% depending on distance and arrangement of source and additional cavities.

Seismograms recorded during the Non-Proliferation Experiment exhibit a strong variation in their signals as a function of receiver location. We calculated some of these traces using a simplified 2-D model of the underground test site. We found that the transverse component matches the observed data fairly well around the arrival time of S-waves generated by cavities in the near-field of the source. However, early arrivals on the transverse component are due to the scattering of P-waves by near-receiver heterogeneities. Similarly, S-waves generated near the source scatter from the transverse component into the radial one.

We believe that near-source heterogeneities have a strong effect on the radiation patterns and waveforms received at larger distances. However, these results were obtained from a 2-D model. In 2-D, an extended cavity acts as a barrier. In 3-D, the cavity is just a scatterer. Hence, we expect some differences between the 2-D model and the 3-D experiment. In the future, we plan to expand the MMP method from 2-D to 3-D which will allow us to address these issues more rigorously.

## Acknowledgments

This work was supported by the Air Force Technical Applications Center/Phillips Laboratory under Contract No. F19628-95-C-0091.

## Appendix A Elastic Multiple Multipole Expansions

The calculations in this paper are done using a multiple multipole expansion method (Imhof, 1996). This appendix presents an introduction to the method. The medium is assumed to be a homogeneous fullspace with  $D$  embedded cavities. In the frequency domain, the displacement  $\mathbf{u}(\mathbf{x}, \omega) e^{i\omega t}$  of an elastic P-SV wave travelling in the two-dimensional, homogeneous region is described by (Pao and Mow, 1973)

$$\frac{1}{k^2} \nabla \nabla \cdot \mathbf{u} - \frac{1}{l^2} \nabla \times \nabla \times \mathbf{u} + \mathbf{u} = 0 \quad (\text{A-1})$$

where we suppressed the harmonic time factor  $e^{i\omega t}$ . We also introduced the wave numbers  $k = \omega/v_p$  and  $l = \omega/v_s$  for a particular frequency  $\omega$ , P-wave velocity  $v_p$ , and S-wave velocity  $v_s$ .

Instead of using the displacement  $\mathbf{u}(\mathbf{x}, \omega)$  directly, we separate it into parts (Pao and Mow, 1973; Imhof, 1996):

$$\mathbf{u}(\mathbf{x}, \omega) = \mathbf{u}^\Phi(\mathbf{x}, \omega) + \mathbf{u}^\Psi(\mathbf{x}, \omega) + \mathbf{u}^{inc}(\mathbf{x}, \omega) + \mathbf{u}^\epsilon(\mathbf{x}, \omega). \quad (\text{A-2})$$

The first term denotes the P-waves generated by the cavities. Similarly, the second term denotes the S-waves radiated by the cavities. The third term  $\mathbf{u}^{inc}(\mathbf{x}, \omega)$  is used for sources outside the cavities, or incident wavefields which are known. Because  $\mathbf{u}^\Phi$  and  $\mathbf{u}^\Psi$  depend on the geometry of

the cavities and the source mechanism, we will expand them into multiple multipole series. We will need to truncate the expansions after a finite number of terms. Therefore, we also add an error term  $\mathbf{u}^\epsilon$  to (A-2).

The displacement fields  $\mathbf{u}^\Phi$  and  $\mathbf{u}^\Psi$  are expanded as follows:

$$\mathbf{u}^\Phi(\mathbf{x}, \omega) = \sum_{d=1}^D \sum_{p=1}^{P_d} \sum_{n=-N}^{+N} a_{pnd} \mathbf{u}_{pnd}^\Phi(\mathbf{x}, \mathbf{x}_{pd}, k, \omega), \quad (\text{A-3a})$$

$$\mathbf{u}^\Psi(\mathbf{x}, \omega) = \sum_{d=1}^D \sum_{p=1}^{P_d} \sum_{n=-N}^{+N} b_{pnd} \mathbf{u}_{pnd}^\Psi(\mathbf{x}, \mathbf{x}_{pd}, l, \omega), \quad (\text{A-3b})$$

where  $a_{pnd}$  and  $b_{pnd}$  are yet unknown weighting coefficients. The expansion functions  $\mathbf{u}_{pnd}^\Phi$  and  $\mathbf{u}_{pnd}^\Psi$  are solutions to (A-1). We have an expansion for each cavity  $1 \leq d \leq D$ . In each cavity  $d$ , we place  $P_d$  different multipoles of orders  $-N$  to  $+N$  centered at  $\mathbf{x}_{pd}$ . Each summation over  $n$  corresponds to a multipole. Because we have more than one multipole per cavity, the scheme is named multiple multipoles expansion. The expansion functions are defined as:

$$\mathbf{u}_{pnd}^\Phi(\mathbf{x}, \mathbf{x}_{pd}, k, \omega) = \nabla H_{|n|}^{(1)}(k |\mathbf{x} - \mathbf{x}_{pd}|) e^{in\vartheta_{pd}} \quad (\text{A-4a})$$

$$\mathbf{u}_{pnd}^\Psi(\mathbf{x}, \mathbf{x}_{pd}, l, \omega) = \nabla \times \hat{\mathbf{y}} H_{|n|}^{(1)}(l |\mathbf{x} - \mathbf{x}_{pd}|) e^{in\vartheta_{pd}} \quad (\text{A-4b})$$

Each expansion function of (A-4) satisfies the wave equation (A-1). For each function, e.g.  $\mathbf{u}_{pnd}^\Phi$ , we obtain the corresponding stress tensor  $\mathbf{T}_{pnd}^\Phi$ :

$$\mathbf{T}_{pnd}^\Phi = \frac{1}{2} \mathbf{C} : (\nabla \mathbf{u}_{pnd}^\Phi + \mathbf{u}_{pnd}^\Phi \nabla), \quad (\text{A-5})$$

where  $\mathbf{C}$  is a fourth-order tensor containing the elastic parameters (Ben-Menahem and Singh, 1981). On the boundary of the cavities, the total traction  $\mathbf{t}(\mathbf{x}, \omega) = \mathbf{T}(\mathbf{x}, \omega) \cdot \hat{\mathbf{n}}(\mathbf{x})$  has to vanish. Thus, we find a linear set of equations by satisfying the boundary condition on discrete matching points  $\mathbf{x}$  at the boundary of the cavities. Along each cavity  $d$ , we have:

$$\mathbf{t}^{inc}(\mathbf{x}, \omega) + \sum_{d=1}^D \sum_{p=1}^{P_d} \sum_{n=-N}^{+N} \left\{ a_{pnd} \mathbf{t}_{pnd}^\Phi(\mathbf{x}, \omega) + b_{pnd} \mathbf{t}_{pnd}^\Psi(\mathbf{x}, \omega) \right\} + \mathbf{t}^\epsilon = \mathbf{t}_d^{src}(\mathbf{x}, \omega) \quad (A-6)$$

where we included a prescribed traction  $\mathbf{t}_d^{src}(\mathbf{x}, \omega)$  along the boundary of cavity  $d$ . We can use this to include instantaneous pressurization sources into our models. Thus, sources can be represented either by an incident wavefield  $\mathbf{u}^{inc}(\mathbf{x}, \omega)$  and its conjugate tractions  $\mathbf{t}^{inc}(\mathbf{x}, \omega)$  or by prescribing the traction  $\mathbf{t}_d^{src}(\mathbf{x}, \omega)$  along the cavity  $d$ . For simple models, either  $\mathbf{u}^{inc}(\mathbf{x}, \omega)$  or  $\mathbf{t}_d^{src}(\mathbf{x}, \omega)$  vanishes. Generally, the resulting system of linear equation needs to be solved in the least-squares sense by choosing more matching points than expansion functions.

## Appendix B Moment Tensor from Multiple Multipole Expansions

MMP-expansions of the form (A-3) are useful for numerical calculations. However, we can also translate them into a more traditional moment tensor expansion which is routinely calculated from observed data (e.g. Patton, 1991). Graf's theorem (also called addition theorem: Abramowitz and Stegun, 1964, Eqn. 9.1.79) allows us to move an expansion function to the origin. The different angles and vectors are defined in Figure 18.

$$H_{|n|}(k |\mathbf{x} - \mathbf{x}_{pd}|) e^{in\vartheta_{pd}} = \sum_{m=-\infty}^{+\infty} s(n) s(n-m) s(m) J_{|n-m|}(k |\mathbf{x}_{pd}|) e^{-i(n-m)\theta_{pd}} H_{|m|}(k |\mathbf{x}|) e^{im\vartheta} \quad (B-1)$$

Because we chose a different normalization of the Hankel functions, we need to include additional sign functions  $s(n)$  defined as  $s(n) = 1$  for  $n \geq 0$  and  $s(n) = (-1)^n$  for  $n < 0$ .  $J_{|n|}(kr)$  denotes the Bessel function of order  $n$ . The above version of the translation theorem is only valid for

$|\mathbf{x}| > |\mathbf{x}_{pd}|$ . Thus, we move the complete right-hand side of (A-3) to the origin which collapses the MMP expansions into simple multipole (SMP) expansions valid in the far-field.

$$\sum_{d=1}^D \sum_{p=1}^{P_d} \sum_{n=-N}^{+N} \left\{ a_{pnd} \nabla H_{|n|}(k |\mathbf{x} - \mathbf{x}_{pd}|) e^{in\vartheta_{pd}} + b_{pnd} \nabla \times \hat{\mathbf{y}} H_{|n|}(l |\mathbf{x} - \mathbf{x}_{pd}|) e^{in\vartheta_{pd}} \right\} = \\ \sum_{m=-\infty}^{+\infty} \left\{ \alpha_m \nabla H_{|m|}(k |\mathbf{x}|) e^{im\vartheta} + \beta_m \nabla \times \hat{\mathbf{y}} H_{|m|}(l |\mathbf{x}|) e^{im\vartheta} \right\} \quad (\text{B-2})$$

In the far-field, the wavefield can also be expressed by a moment tensor (MT) expansion (Backus and Mulcahy, 1976a,b) describing the source. However, the MT expansion corresponds only to one-half of the SMP expansion (B-2). The other one-half of (B-2) correspond to torques and non-physical force-systems. They are non-physical because they violate the underlying linear wave theory. Their P- and S-radiation patterns are aligned. In contrast, the patterns are interlaced for physical force systems. The Green's dyadic  $\mathbf{G}(\mathbf{x}, \omega)$  for a source at the origin is defined to be (Ben-Menahem and Singh, 1981)

$$\mathbf{G}(\mathbf{x}, \omega) = \frac{1}{\rho\omega^2} \left\{ l^2 \mathbf{I} \psi(\mathbf{x}) + \nabla \nabla [\psi(\mathbf{x}) - \phi(\mathbf{x})] \right\}, \quad (\text{B-3})$$

where  $\mathbf{I}$  is the identity tensor.  $\phi(\mathbf{x})$  and  $\psi(\mathbf{x})$  denote the scalar Green's functions:

$$\phi(\mathbf{x}) = \frac{i}{4} H_0(k |\mathbf{x}|), \quad \psi(\mathbf{x}) = \frac{i}{4} H_0(l |\mathbf{x}|). \quad (\text{B-4})$$

By orthogonality, we define another dyadic  $\tilde{\mathbf{G}}(\mathbf{x}, \omega)$ :

$$\tilde{\mathbf{G}}(\mathbf{x}, \omega) = \frac{1}{\rho\omega^2} \tilde{\mathbf{I}} \cdot \nabla \nabla \psi(\mathbf{x}) \quad \text{where} \quad \tilde{\mathbf{I}} = \begin{pmatrix} 0 & -1 \\ 1 & 0 \end{pmatrix}. \quad (\text{B-5})$$

Using  $\mathbf{G}(\mathbf{x}, \omega)$  and  $\tilde{\mathbf{G}}(\mathbf{x}, \omega)$ , we write the wavefield  $\mathbf{u}(\mathbf{x}, \omega)$  as:

$$\begin{aligned}\mathbf{u}(\mathbf{x}, \omega) = & \nabla \mathbf{G}(\mathbf{x}, \omega) \cdot \mathbf{I}p(\omega) + \nabla \mathbf{G}(\mathbf{x}, \omega) \cdot \tilde{\mathbf{I}}\tilde{s}(\omega) + \\ & \mathbf{G}(\mathbf{x}, \omega) \cdot \mathbf{f}(\omega) + \tilde{\mathbf{G}}(\mathbf{x}, \omega) \cdot \tilde{\mathbf{f}}(\omega) + \\ & \nabla \mathbf{G}(\mathbf{x}, \omega) \cdot \mathbf{M}(\omega) + \nabla \tilde{\mathbf{G}}(\mathbf{x}, \omega) \cdot \tilde{\mathbf{M}}(\omega) + \dots \quad (\text{B-6})\end{aligned}$$

$p$  corresponds to an explosion source,  $\tilde{\mathbf{f}}$  is a point force. Each quantity with a tilde is either a non-observed source-type ( $\tilde{s}$  corresponds to a torque), or are non-physical, mathematical constructs without application in seismology. Both moment tensors  $\mathbf{M}(\omega)$  and  $\tilde{\mathbf{M}}(\omega)$  are symmetric and deviatoric:

$$\mathbf{M}(\omega) = \begin{pmatrix} m(\omega) & n(\omega) \\ n(\omega) & -m(\omega) \end{pmatrix} \quad \tilde{\mathbf{M}}(\omega) = \begin{pmatrix} \tilde{m}(\omega) & \tilde{n}(\omega) \\ \tilde{n}(\omega) & -\tilde{m}(\omega) \end{pmatrix} \quad (\text{B-7})$$

$m$  and  $n$  correspond to two double-couple systems which are rotated by  $45^\circ$  with respect to each other. The evaluation of (B-6) yields that the first two terms depend only on Hankel functions of zeroth order. The next two terms depend on Hankel functions of the first order, and the final two terms depend on Hankel functions of the second order. Thus, we can equate (B-2) and (B-6) which allows us to find linear relations between  $(\alpha_0, \beta_0)$  and  $(p, \tilde{s})$ , between  $(\alpha_{\pm 1}, \beta_{\pm 1})$  and  $(f_1, f_2, \tilde{f}_1, \tilde{f}_2)$ , and between  $(\alpha_{\pm 2}, \beta_{\pm 2})$  and  $(m, n, \tilde{m}, \tilde{n})$ .

$$p = -4i \frac{\rho \omega^2}{k^2} \alpha_0 \quad (\text{B-8a})$$

$$\tilde{s} = -4i \frac{\rho \omega^2}{l^2} \beta_0 \quad (\text{B-8b})$$

$$f_1 = (2 + 2i) \frac{\rho\omega^2}{kl} \{ k(i\beta_{+1} + \beta_{-1}) - l(i\alpha_{+1} + \alpha_{-1}) \} \quad (\text{B-9a})$$

$$f_2 = (2 + 2i) \frac{\rho\omega^2}{kl} \{ l(\alpha_{+1} + i\alpha_{-1}) - k(\beta_{+1} + i\beta_{-1}) \} \quad (\text{B-9b})$$

$$\tilde{f}_1 = (2 + 2i) \frac{\rho\omega^2}{kl} \{ l(\alpha_{+1} + i\alpha_{-1}) + k(i\beta_{+1} + \beta_{-1}) \} \quad (\text{B-9c})$$

$$\tilde{f}_2 = (2 + 2i) \frac{\rho\omega^2}{kl} \{ l(i\alpha_{+1} + \alpha_{-1}) - k(\beta_{+1} + i\beta_{-1}) \} \quad (\text{B-9d})$$

$$m = -(2 + 2i) \frac{\rho\omega^2}{k^2 l^2} \{ k^2(i\beta_{+2} + \beta_{-2}) - l^2(i\alpha_{+2} + \alpha_{-2}) \} \quad (\text{B-10a})$$

$$n = -(2 + 2i) \frac{\rho\omega^2}{k^2 l^2} \{ l^2(\alpha_{+2} + i\alpha_{-2}) - k^2(\beta_{+2} + i\beta_{-2}) \} \quad (\text{B-10b})$$

$$\tilde{m} = -(2 + 2i) \frac{\rho\omega^2}{k^2 l^2} \{ l^2(\alpha_{+2} + i\alpha_{-2}) + k^2(i\beta_{+2} + \beta_{-2}) \} \quad (\text{B-10c})$$

$$\tilde{n} = -(2 + 2i) \frac{\rho\omega^2}{k^2 l^2} \{ l^2(i\alpha_{+2} + \alpha_{-2}) - k^2(\beta_{+2} + i\beta_{-2}) \} \quad (\text{B-10d})$$

Once a solution to a problem is obtained by solving the linear system for the weighting coefficients  $a_{pnd}$  and  $b_{pnd}$ , it can be converted to a moment tensor using relations (B-8), (B-9), and (B-10). The moment tensor can directly be used to show the frequency dependence of the different components. Alternatively, the results can be Fourier transformed to yield the source-time history as presented in Figures 10 and 13.

## References

Abramowitz, M. and Stegun, I. A., editors (1964). *Handbook of Mathematical Functions*. Dover, New York.

App, F. N. and Brunish, W. M. (1991). Stress wave calculations for four selected underground nuclear tests: MERLIN, HEARTS, PRESIDIO, MISTY ECHO. Technical Report EES-NTC-91-03, Los Alamos National Laboratory.

App, F. N., Bos, R. J., Dey, T. N., Jones, E. M., Kamm, J. R., and Taylor, S. R. (1995). Examining near-source effects in the far field. In J. Lewkowitz, editor, *Proceedings of the 17th Annual Seismic Research Symposium on Monitoring a Comprehensive Test Ban Treaty*, PL-TR-95-2108, pages 609–616. Phillips Laboratory, ADA310037.

Backus, G. and Mulcahy, M. (1976a). Moment tensors and other phenomenological description of seismic sources – I. continuous displacements. *Geophys. J. R. Astron. Soc.*, **46**, 341–361.

Backus, G. and Mulcahy, M. (1976b). Moment tensors and other phenomenological description of seismic sources – II. discontinuous displacements. *Geophys. J. R. Astron. Soc.*, **47**, 301–329.

Baldwin, M. J., Bradford, R. P., Hopkins, S. P., Townsend, D. R., and Harris-West, B. L. (1994). Geology, geophysics, and physical properties of the U12n.25 Non-Proliferation Experiment site. In M. D. Denny and S. P. Stull, editors, *Proceedings of the symposium on the Non-Proliferation Experiment (NPE): Results and implications for test ban treaties*, CONF-9404100. Lawrence Livermore National Laboratory.

Ben-Menahem, A. and Mikhailov, O. (1995). Multiple radiation of seismic waves from explosions in non-spherical cavities and its application to signal identification. *J. Acoust. Soc. Am.*, **97**(5), 2675–2698.

Ben-Menahem, A. and Singh, S. J. (1981). *Seismic Waves and Sources*. Springer, New York.

Bennett, T. J., McLaughlin, K. L., Marshall, M. E., Barker, B. W., and Murphy, J. R. (1995). Investigations of the seismic characteristics of rockbursts. Technical Report PL-TR-95-2169 (SSS-DPR-95-15259), Phillips Laboratory, ADA304549.

Blandford, R. R. (1981). Seismic discrimination problems at regional distances. In E. S. Husebye and S. Mykkeltveit, editors, *Identification of Seismic Sources - Earthquake or Underground Explosion*, pages 695–740. D. Reidell Publishing Company, Boston.

Denny, M. D. and Stull, S. P., editors (1994). *Proceedings of the symposium on the Non-Proliferation Experiment (NPE): Results and implications for test ban treaties*, CONF-9404100. Lawrence Livermore National Laboratory.

Gibson, R. L., Toksöz, M. N., and Dong, W. (1996). Seismic radiation from explosively loaded cavities in isotropic and transversely isotropic media. *Bull. Seismol. Soc. Am.*, **86**(6), 1910–1924.

Glenn, L. A. and Rial, J. A. (1987). Blast wave effects on decoupling with axisymmetric cavities. *Geophys. J. R. Astron. Soc.*, **91**, 229–239.

Haskell, N. A. (1967). Analytic approximation for the elastic radiation from a contained underground explosion. *J. Geophys. Res.*, **72**(10), 2583–2587.

Imhof, M. G. (1996). Multiple multipole expansions for elastic scattering. *J. Acoust. Soc. Am.*, **100**(5), 2969–2979.

Johnson, L. R. (1995). The effect of near-receiver scattering on seismograms. In J. Lewkowitz, editor, *Proceedings of the 17th Annual Seismic Research Symposium on Monitoring a Comprehensive Test Ban Treaty*, PL-TR-95-2108, pages 421–432. Phillips Laboratory, ADA310037.

Johnson, L. R. and McEvilly, T. V. (1994). Near-source observations of the NPE. In J. Lewkowitz, editor, *Proceedings of the 16th Annual Seismic Research Symposium on Monitoring a Comprehensive Test Ban Treaty*, pages 182–188. Phillips Laboratory, PL-TR-94-2217, ADA284667.

Kamm, J. R. and Bos, R. J. (1995). Comparison of chemical and nuclear explosions: numerical simulations of the Non-Proliferation Experiment. Technical Report LA-12942, Los Alamos National Laboratory.

Latter, A. L., LeLevier, R. E., Martinelli, E. A., and McMillan, W. G. (1961). A method of concealing underground nuclear explosions. *J. Geophys. Res.*, **66**(3), 943–946.

Li, Y., Toksöz, M. N., and Rodi, W. L. (1996). Discrimination of small earthquakes and explosions. In J. Lewkowitz, J. M. McPhetres, and D. T. Reiter, editors, *Proceedings of the 18th Annual Seismic Research Symposium on Monitoring a Comprehensive Test Ban Treaty*, PL-TR-96-2153, pages 574–583. Phillips Laboratory, ADA313692.

Murphy, J. R., Kitov, I. O., Rimer, N., Sultanov, D. D., Barker, B. W., and Stevens, J. L. (1995). Analyses of the seismic characteristics of U.S. and Russian cavity decoupled explosions. In

J. Lewkowitz, editor, *Proceedings of the 17th Annual Seismic Research Symposium on Monitoring a Comprehensive Test Ban Treaty*, PL-TR-95-2108, pages 667–676. Phillips Laboratory, ADA310037.

Olsen, K. H. and Peratt, A. L. (1994). Free-field ground motions for the Non-Proliferation Experiment: preliminary comparisons with nearby nuclear events. In M. D. Denny and S. P. Stull, editors, *Proceedings of the symposium on the Non-Proliferation Experiment (NPE): Results and implications for test ban treaties*, CONF-9404100. Lawrence Livermore National Laboratory.

Pao, Y. H. and Mow, C. C. (1973). *Diffraction of Elastic Waves and Dynamic Stress Concentrations*. Crane Russak, New York.

Patton, H. J. (1991). Seismic moment estimation and the scaling of the long-period explosion source spectrum. In S. Taylor, H. Patton, and P. Richards, editors, *Explosion Source Phenomenology*, pages 171–184. American Geophysical Union, Washington, D.C.

Pearson, D. C., Stump, B. W., and Phillips, W. S. (1996). The White Mine explosively induced, controlled collapse experiment. In J. Lewkowitz, J. M. McPhetres, and D. T. Reiter, editors, *Proceedings of the 18th Annual Seismic Research Symposium on Monitoring a Comprehensive Test Ban Treaty*, PL-TR-96-2153, pages 937–946. Phillips Laboratory, ADA313692.

Reamer, S. K., Hinzen, K. G., and Stump, B. W. (1992). Near-source characterization of the seismic wavefield radiated from quarry blasts. *Geophys. J. Int.*, **110**(3), 435–450.

Rial, J. A. and Moran, B. (1986). Radiation patterns for explosively-loaded axisymmetric cavities in an elastic medium: analytic approximations and numerical results. *Geophys. J. R. Astron. Soc.*, **86**, 855–862.

Stevens, J. L., Rimer, N., Murphy, J., Barker, T. G., Bailey, E., Halda, E. J., Proffer, W. J., Rogers, S. H., and Shkoller, B. (1991). Simulation of seismic signals from partially coupled nuclear explosions in spherical and ellipsoidal cavities. Technical Report SSS-FR-91-12735, MAXWELL S-CUBED Division. Final Report on Contract No. 90-N3039000-000.

Stump, B. W., Pearson, D. C., and Reinke, R. E. (1994). Source comparison between nuclear and chemical explosions detonated at Rainier Mesa, Nevada Test Site. Technical Report LA-UR-94-4073, Los Alamos National Laboratory.

Zhao, L. and Harkrider, D. G. (1992). Wavefields from an off-center explosion in an embedded solid sphere. *Bull. Seismol. Soc. Am.*, **82**, 1927–1955.

Gauge ID	Range [m]	Azimuth [deg]	Organization	Comment
Q3	821	359	LLNL	Surface
Q5	728	310	LLNL	Surface
S4A	868	248	LANL	Surface
S6P	800	217	LANL	Surface
S10A	789	156	LANL	Surface
E10	558	104	LLNL	Surface
S12P	920	67	LANL	Surface
TM8	438	36	LANL	Freefield
TM9	392	27	LANL	Freefield
TM10	676	38	LANL	Freefield
TM24	475	351	LANL	Freefield

Table I: NPE accelerometer stations used in this paper. Listed are the gauge ID, the radial range from the source, the source-to-station azimuth (degrees East of North), the fielding organization, and an indication whether the gauge was located at the surface or in a cavity at the same depth as source measuring the freefield (Kamm and Bos, 1995).

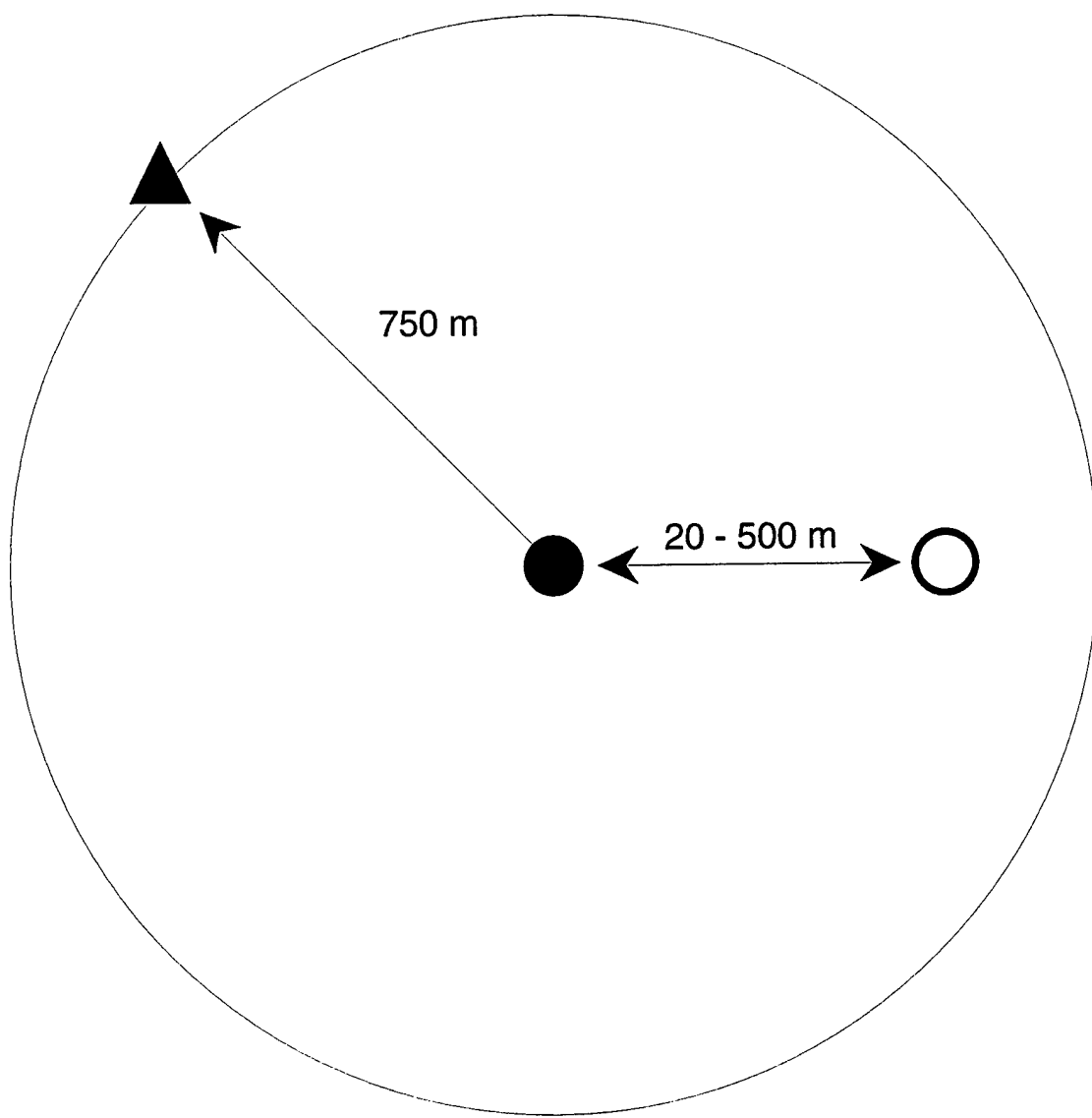


Figure 1: Geometry for the first numerical experiment: a cylindrical cavity is instantaneously pressurized by an explosion. At a certain distance in the near-field, there is a second cavity scattering and converting wave-modes. The total radiation pattern is then measured at a distance of 750 m from the source.

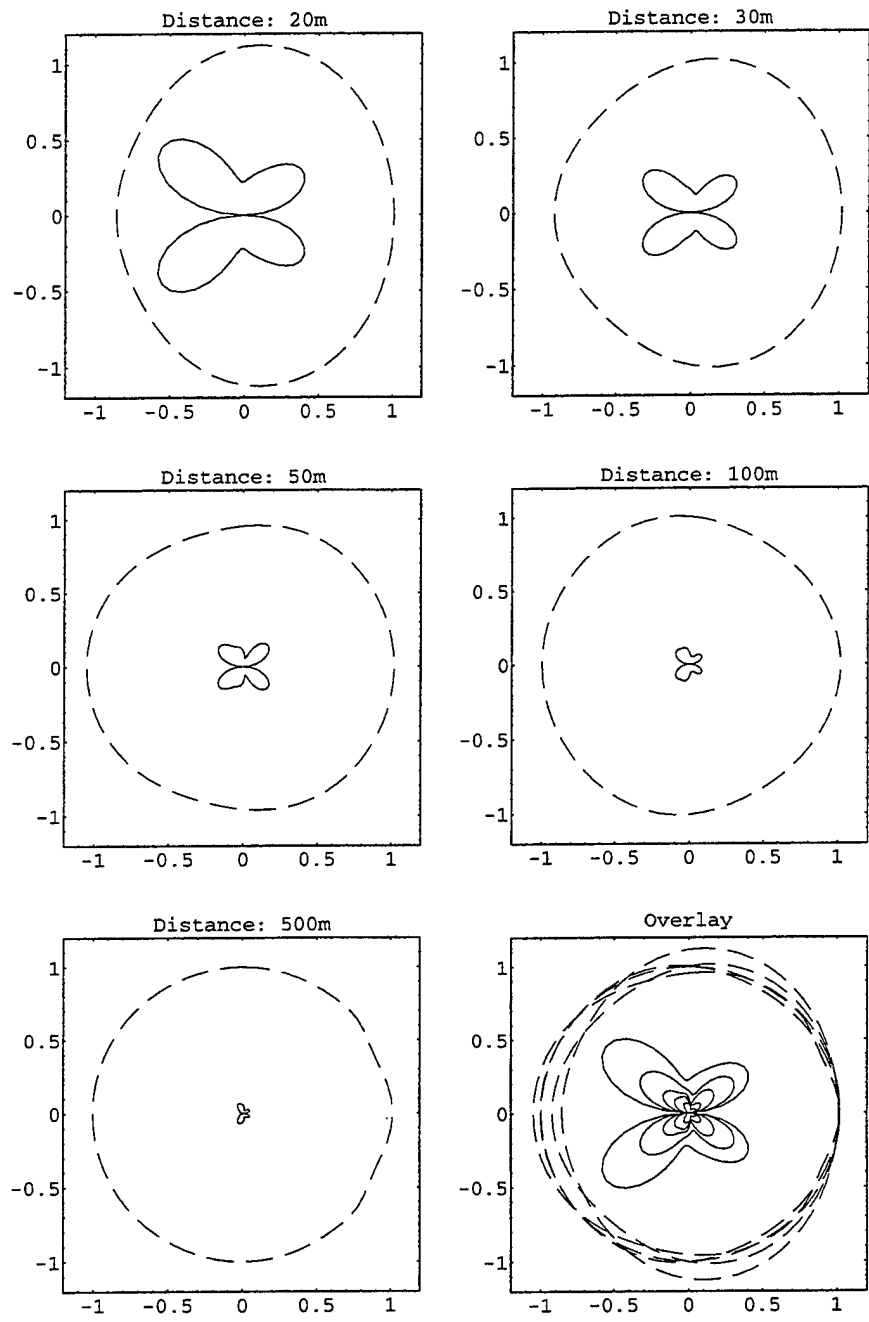


Figure 2: Radiation patterns for P-waves (dashed) and S-waves (solid) as a function of distance between source cavity and additional cavity (scatterer) for the dominant frequency of 10 Hz.

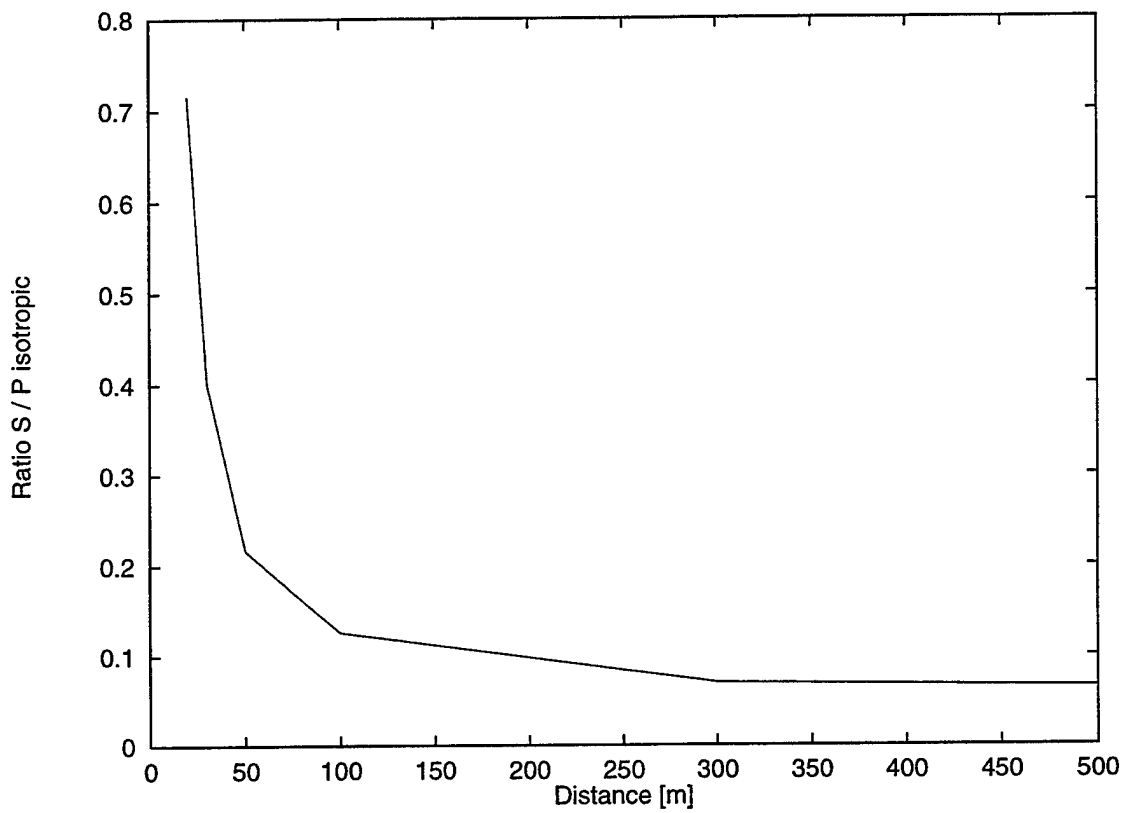


Figure 3: Ratio between the maximum S-wave amplitude and the isotropic P-wave amplitude as a function of distance between the two cavities. The effect of the second cavity decays very fast with increasing separation.

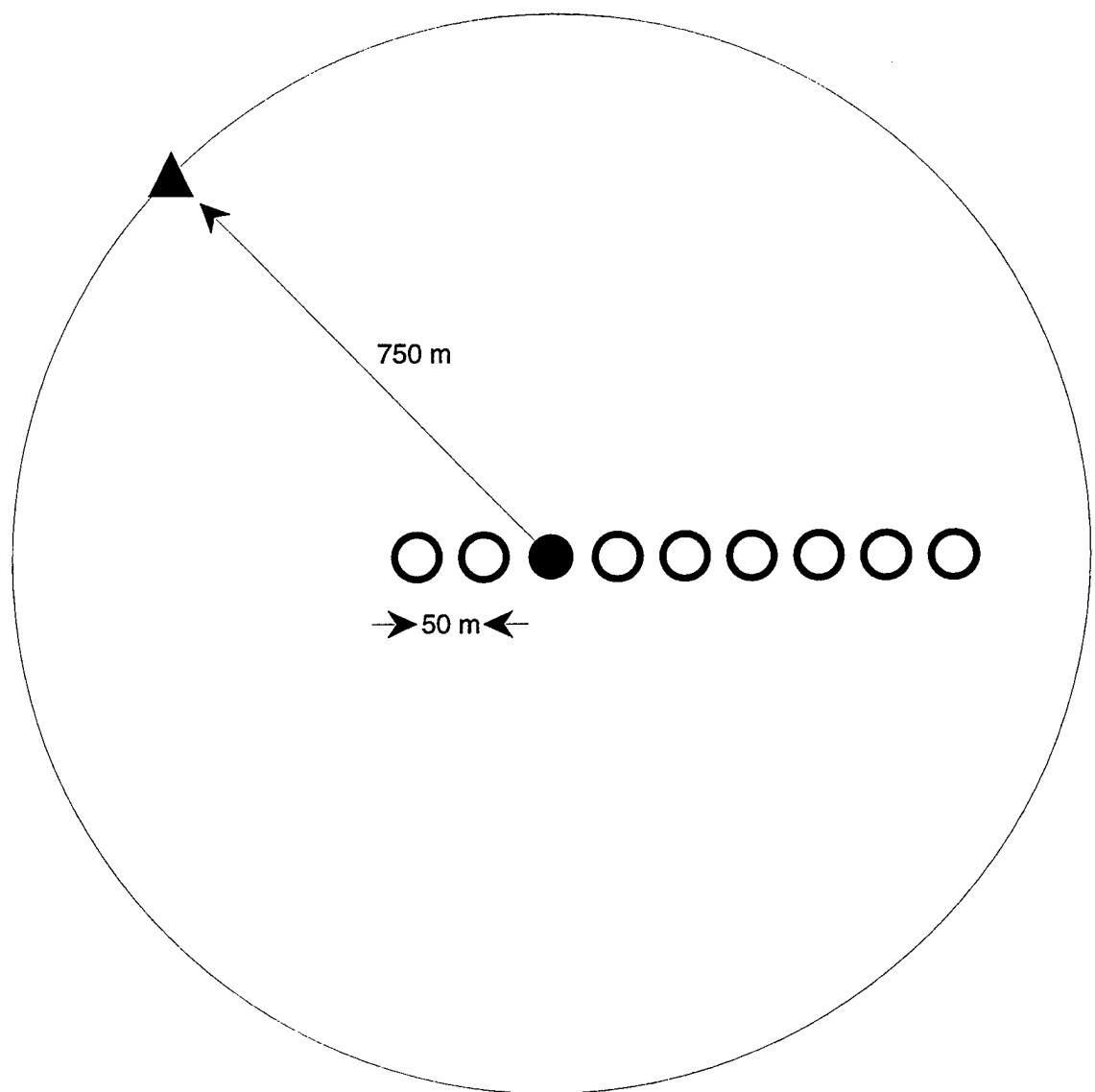


Figure 4: Array of 9 cavities with a spacing of 50 m. Each cavity is used once as a source chamber. The case shown is the third one in the sequence. The total radiation pattern is measured at a distance of 750 m from the source chamber.

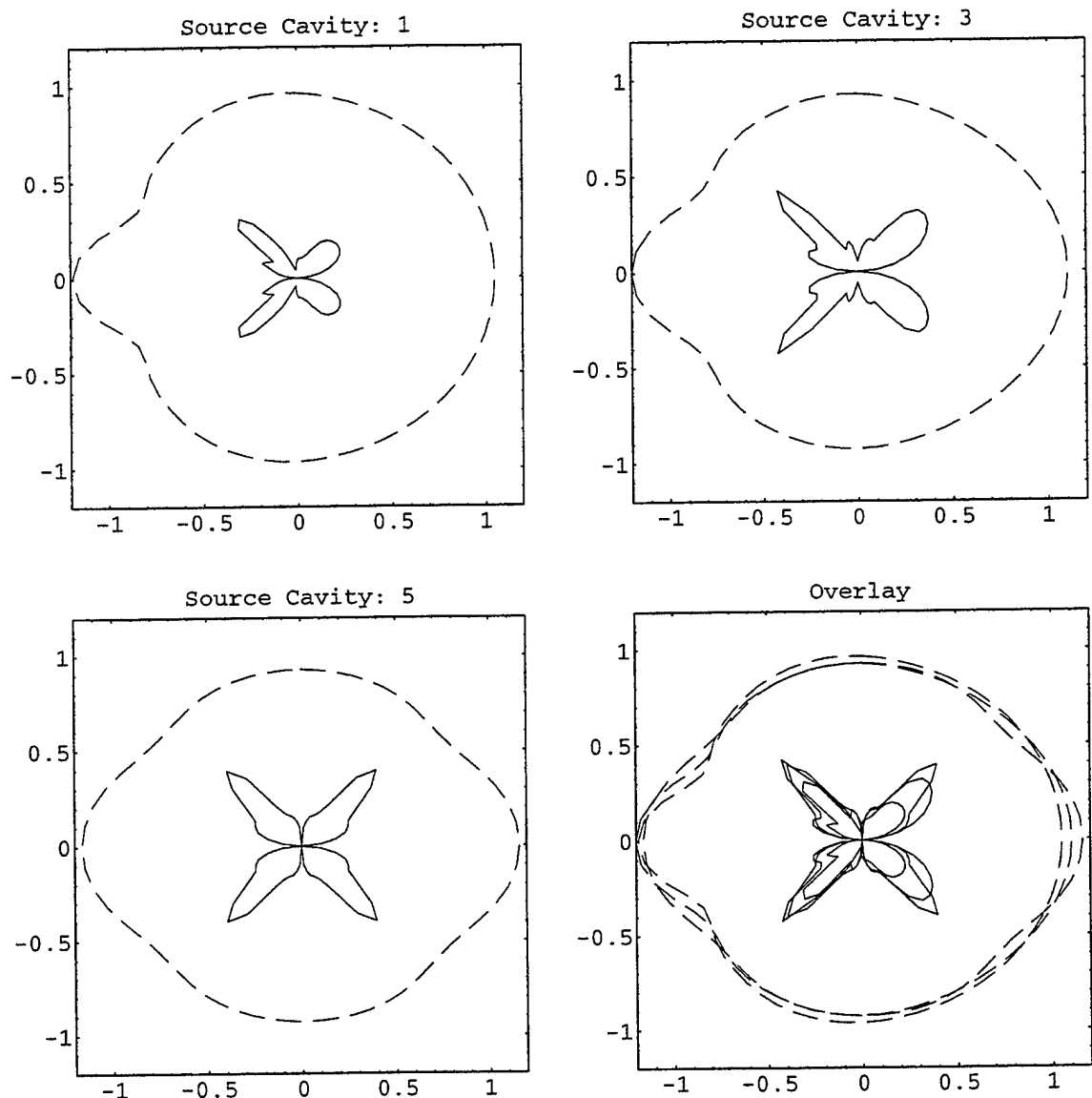


Figure 5: Radiation patterns for P-waves (dashed) and S-waves (solid) as a function of location of the source cavity with respect to additional cavities (scatterers). The patterns are calculated for the dominant frequency of 10 Hz.

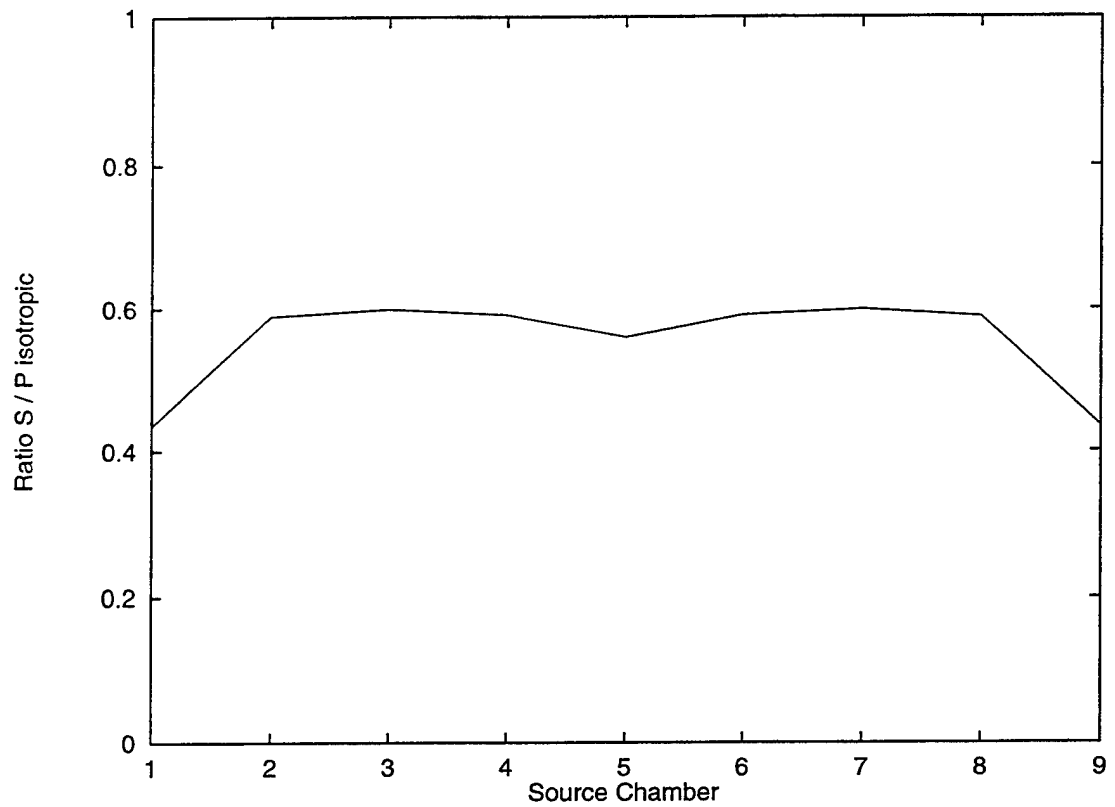


Figure 6: Ratio between the maximum S-wave amplitude and the isotropic P-wave amplitude as a function of source chamber within the array.

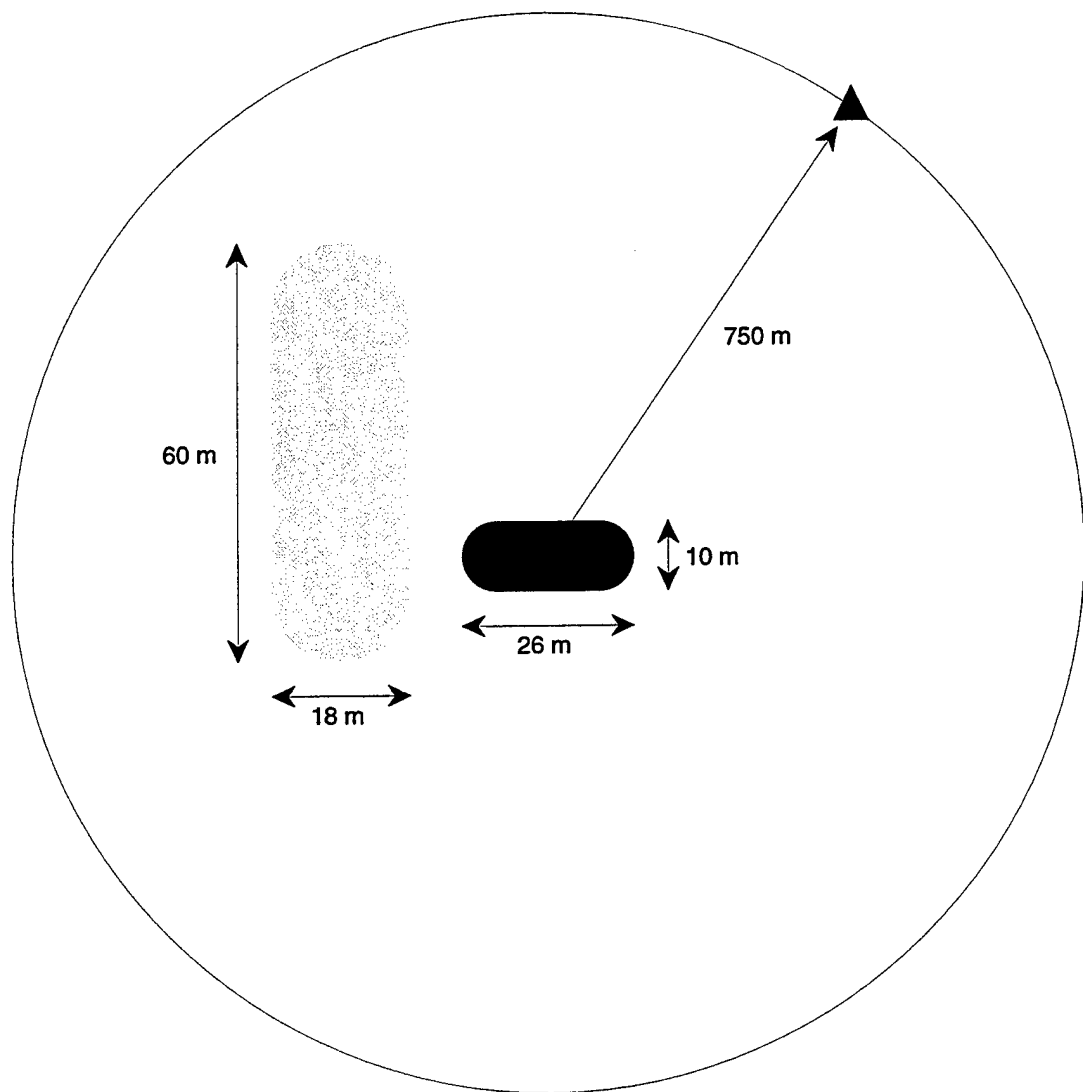
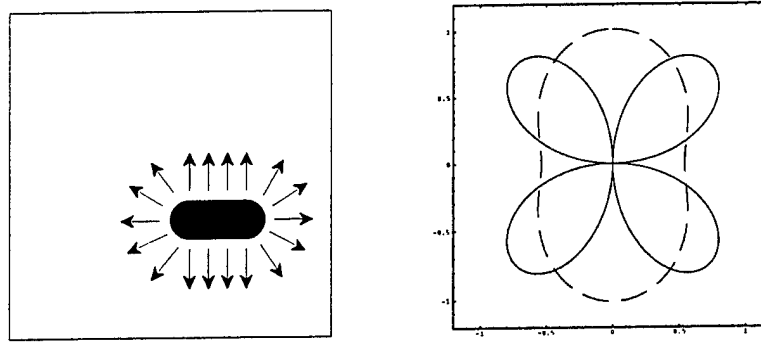
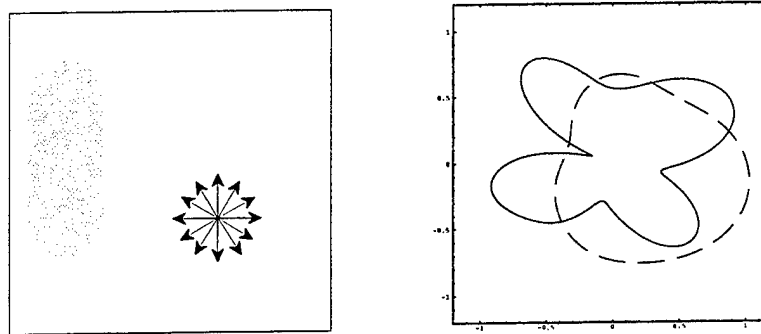


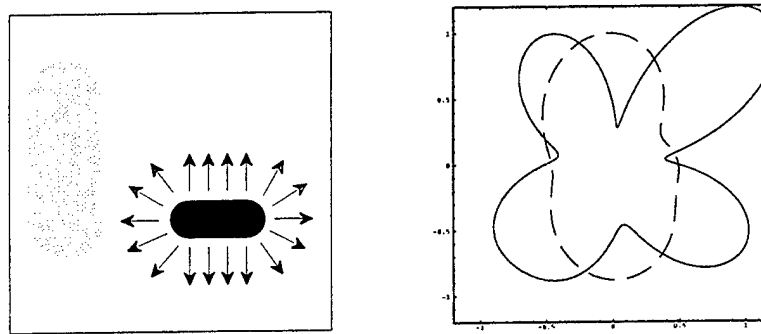
Figure 7: Two oval cavities are embedded in a homogeneous fullspace. Different source mechanisms are tested in this configuration. The black cavity is used for the source.



(a)



(b)



(c)

Figure 8: Radiation patterns for P-waves (dashed) and S-waves (solid): (a) for an instantaneous pressurization of the source cavity, (b) for an isotropic explosion source near a large tunnel, and (c) for an instantaneous pressurization of a source cavity near a large tunnel.

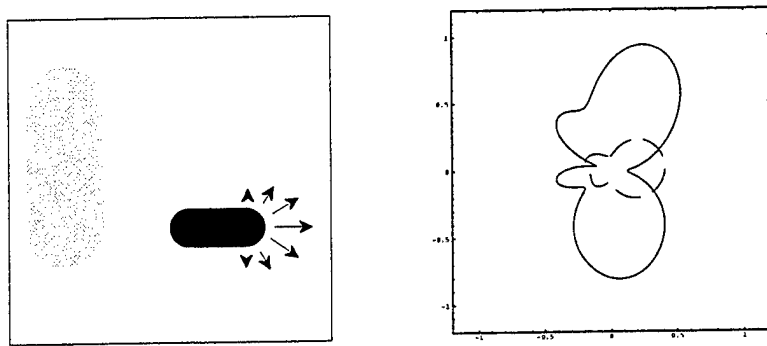


Figure 9: Radiation patterns for P-waves (dashed) and S-waves (solid): The geometry is the same as in Figure 8(c). But the seismic source is an explosion at the front of the source cavity as in an underground mining or construction environment.

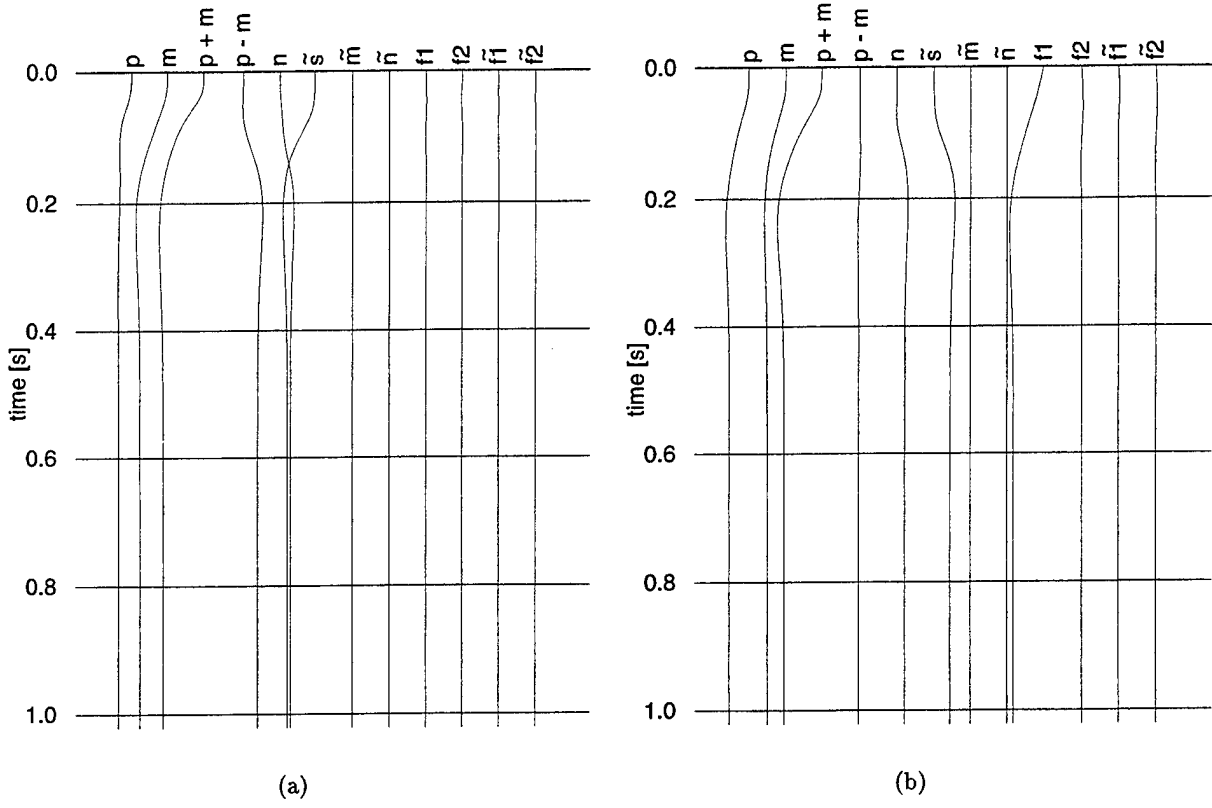


Figure 10: Components of the moment tensor expansion as a function of time for (a) the instantaneous pressurization model shown in Figure 8(c), and (b) the frontal explosion model defined in Figure 9. The components of the moment tensor are explained in Appendix B.

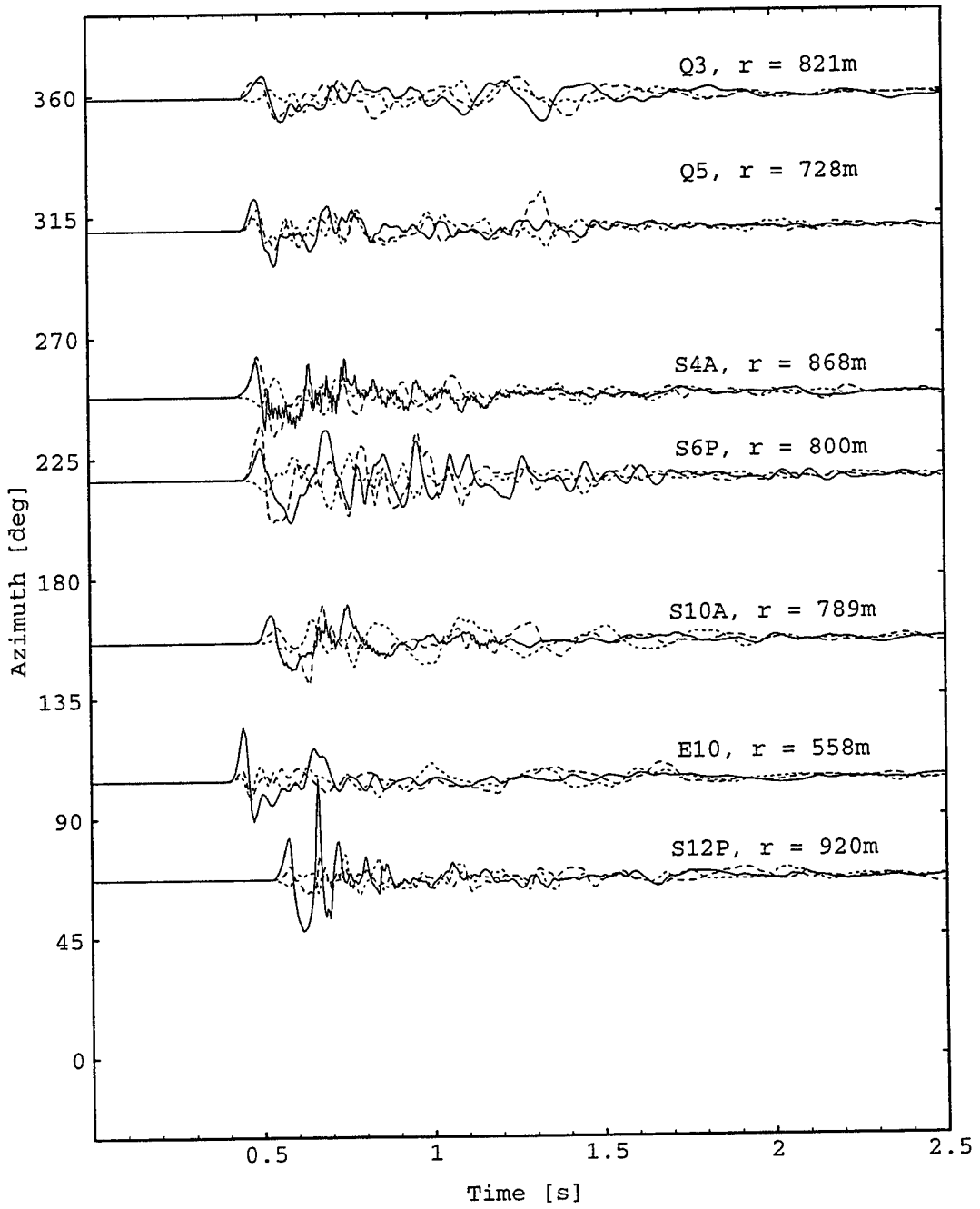


Figure 11: Accelerations recorded at a range of 558 – 920 m from the center of the NPE explosion. Shown are the vertical (solid), radial (dashed), and transverse component (dotted). The data was acquired by LLNL and LANL (Denny and Stull, 1994).

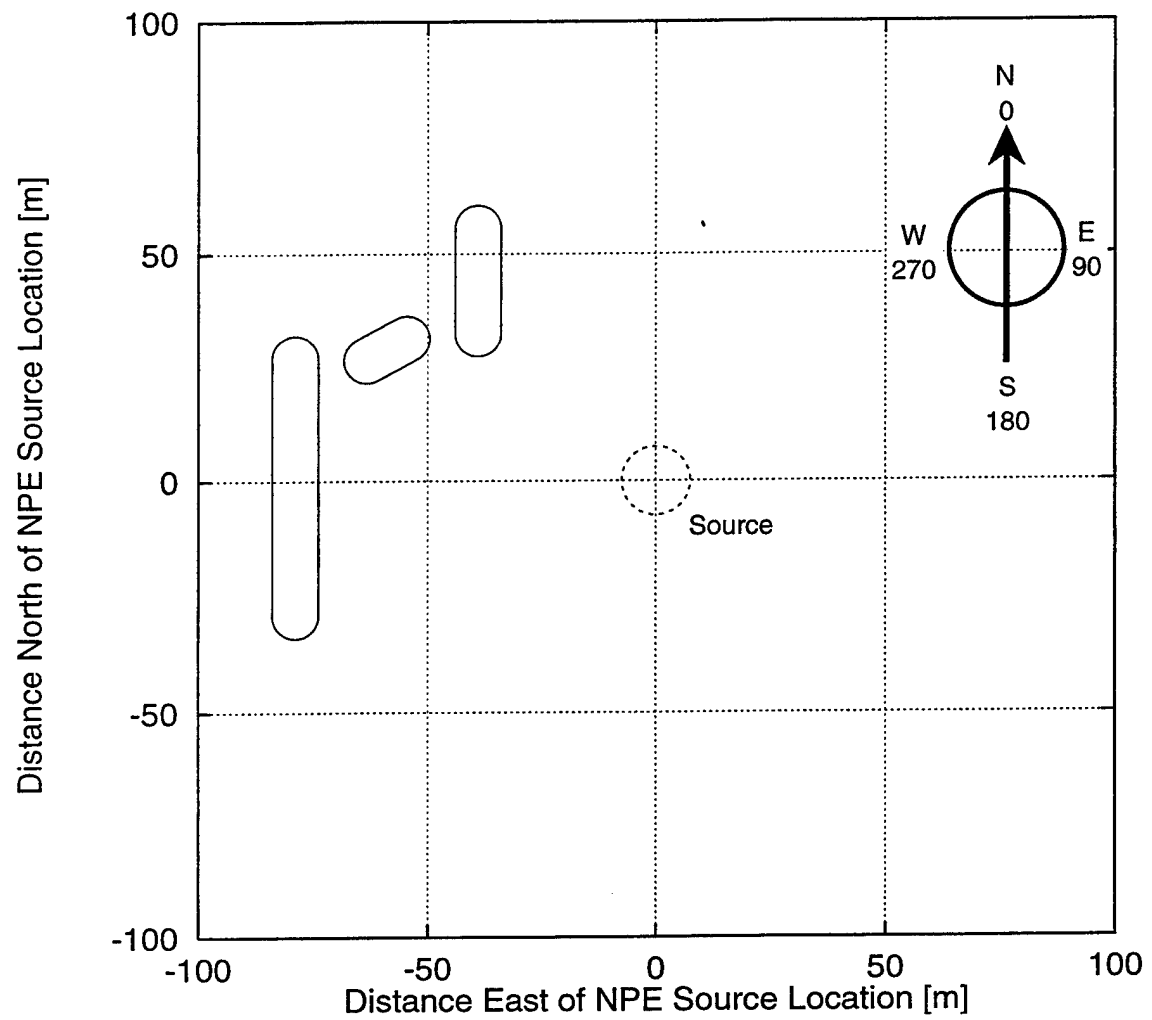


Figure 12: Cavities used for numerical simulation.

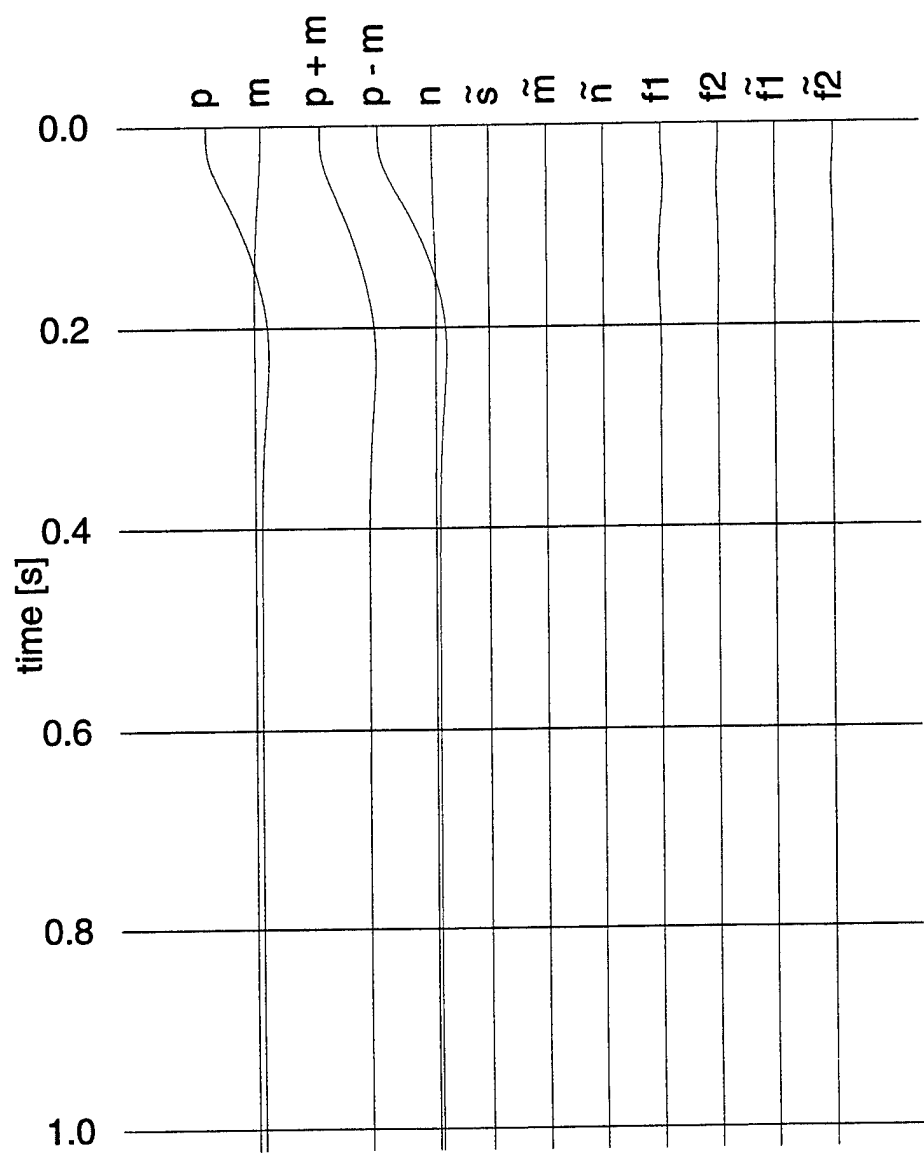
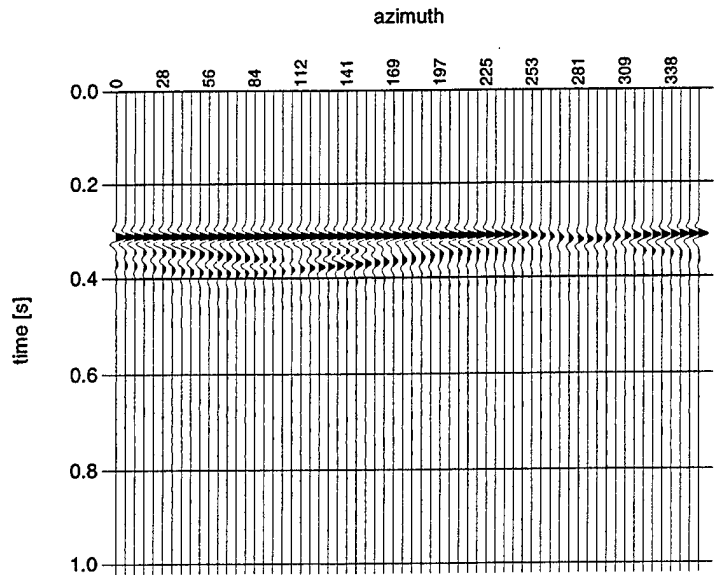
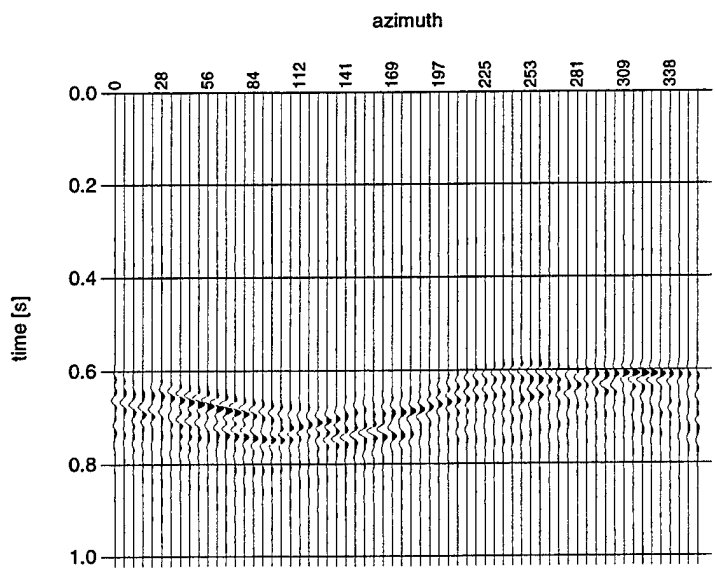


Figure 13: Components of the synthetic NPE moment tensor expansion as a function of time.



(a) radial component



(b) transverse component

Figure 14: The radial and transverse component of the acceleration as calculated for the model shown in Figure 12.

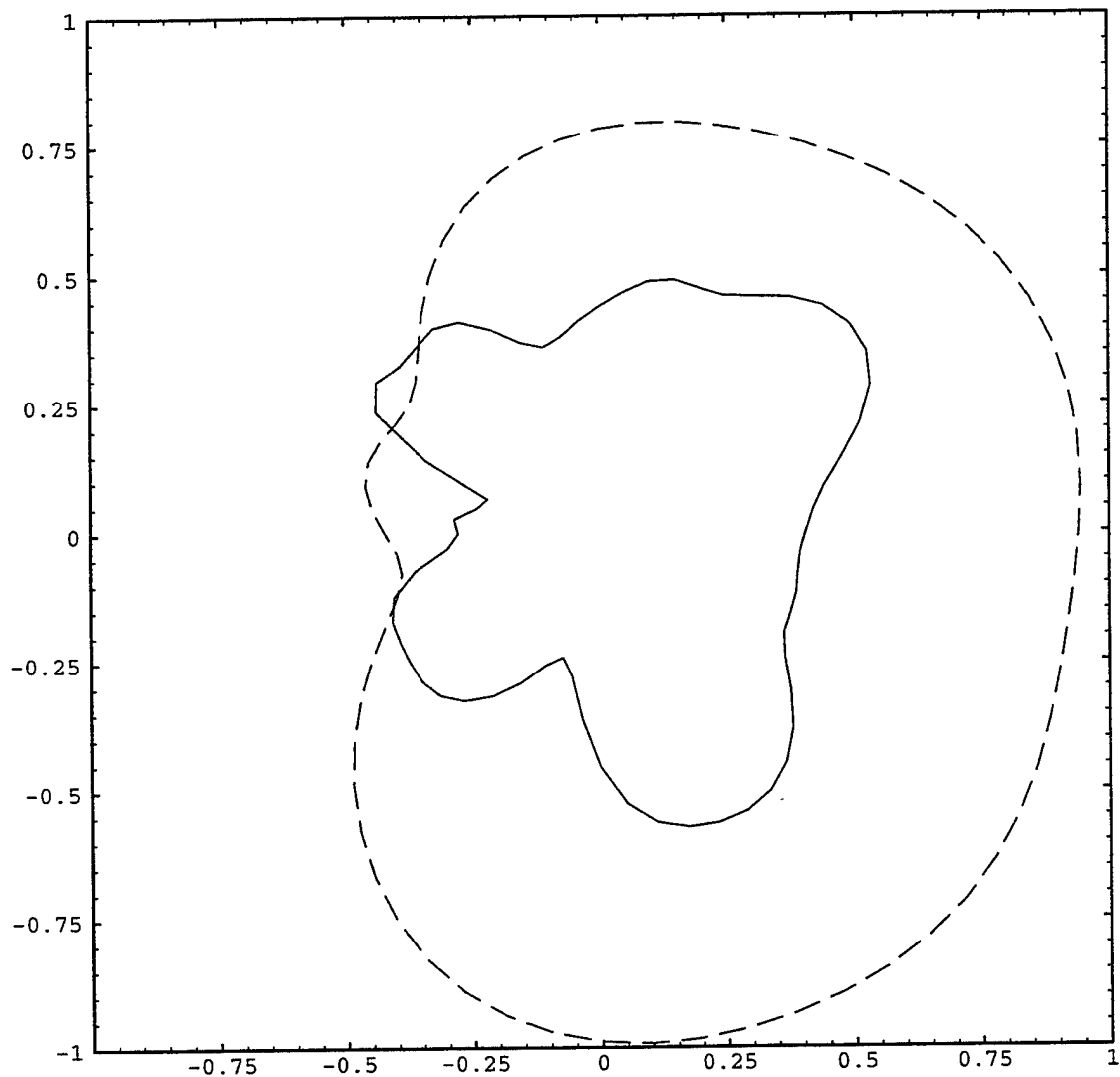


Figure 15: Amplitude as a function of azimuth for the radial component (“P-wave”, dashed) and the transverse component (“S-wave”, solid).

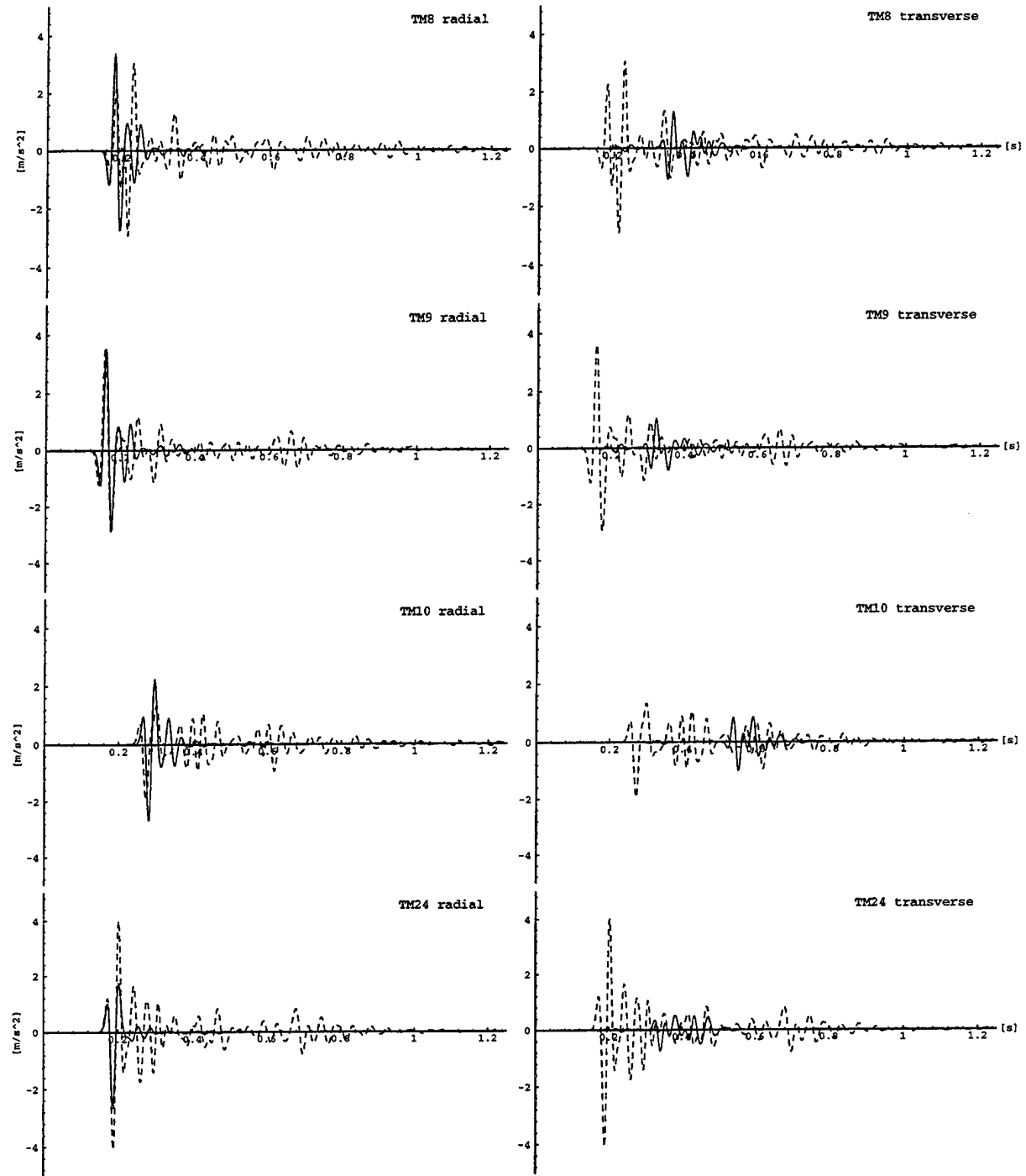


Figure 16: Observed (dashed) and synthetic (solid) accelerations at receiver stations located underground neglecting near-receiver heterogeneities.

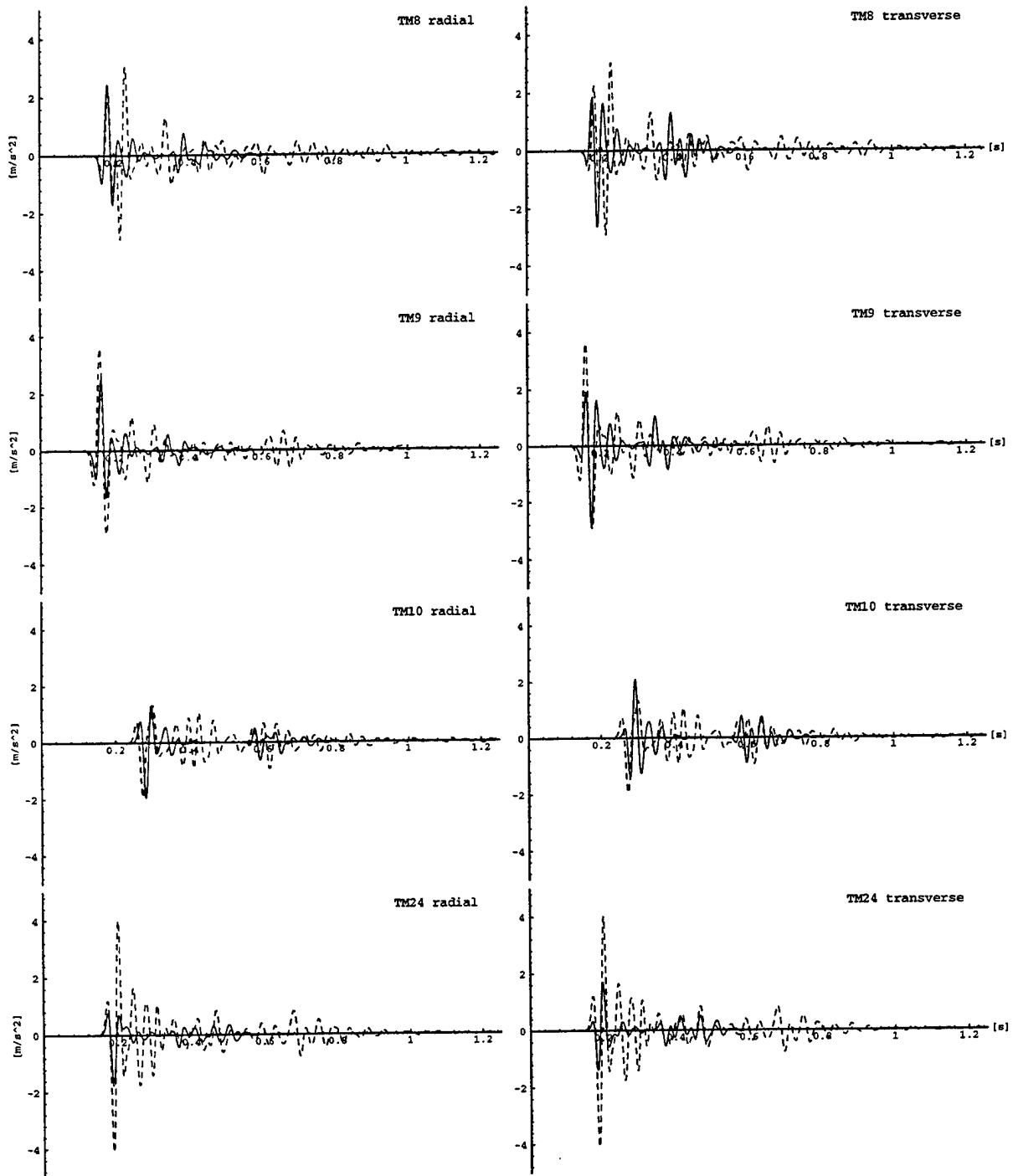


Figure 17: Observed (dashed) and synthetic (solid) accelerations at receiver stations located underground including near-receiver heterogeneities.

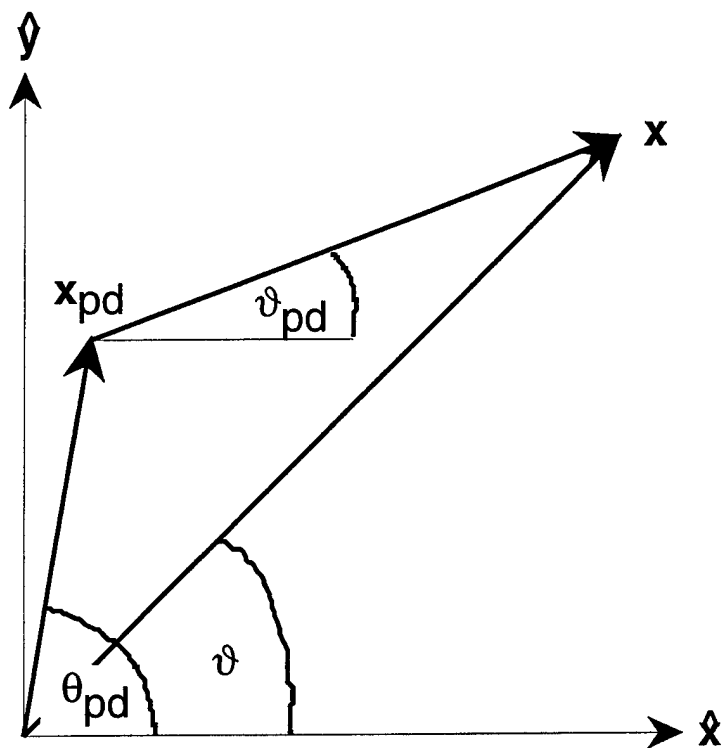


Figure 18: Definition of angles and vectors in Graf's theorem or addition theorem (Abramowitz and Stegun, 1964, Eqn. 9.1.79).

# Simulation of Elastic Wave Propagation in Models Containing Irregular Interfaces Parameterized in Irregular Grids

## Abstract

This study demonstrates the advantages of a recently-developed irregular-grid modeling technique (Nolte *et al.*, 1996). This technique can model irregular interfaces more accurately than a standard regular-grid finite-difference method. We show this by comparison of both methods for a simple model containing a sloping interface. While the discrete approximation to the sloping interface results in numerical inaccuracies for the finite-difference method, the irregular-grid technique produces superior results. We then show that the method can also be applied to a free surface with irregular topography, suggesting that it may be a valuable alternative to existing finite-difference free-surface algorithms. Finally, we demonstrate the effect of irregular surface topography on regional wave propagation with a Middle East example.

## Introduction

It is well known that finite-difference techniques (e.g., Alford *et al.*, 1974; Virieux, 1984, 1986) suffer from inaccuracies in modeling irregular interfaces, due to their discrete approximation to the model. For example, a dipping interface has to be approximated by discrete steps. This approximation can result in diffractions from these “stair steps” (Muir *et al.*, 1992). While these diffractions can often be eliminated by an isotropic interpolation of the medium parameters across the interface, more severe problems occur when larger impedance contrasts are present at an interface. Muir *et al.* (1992) presented an effective-medium approach to model irregular interfaces. Even though there is no rigorous theoretical justification for their approach, their numerical results show that it works well in cases where isotropic interpolation fails. Their method is limited to interfaces with solid material on either side, and thus cannot be applied to an irregular free surface.

Incorporating surface topography into finite-difference modeling codes has been the subject of various previous investigations (e.g., Jih *et al.* 1988; Hestholm and Ruud, 1994; Robertsson, 1996). As shown by Robertsson (1995), various methods have different shortcomings. For example, grid-distortion techniques (Tessmer *et al.*, 1992; Hestholm and Ruud, 1994; Hestholm, 1996) become unstable at steep slopes. Imaging techniques (Levander, 1988; Robertsson, 1996) appear to be more flexible in handling irregular topography. However, Robertsson (1996) was forced to use a very fine gridding in order to avoid the stair-step problems at the free surface. Thus, an accurate representation of an irregular free surface is computationally expensive, and alternative modeling schemes are desirable. One approach could be rectangular variable grid methods (Jastram and Tessmer, 1994; Wang and Schuster, 1996; De Lilla, 1997) combined with Robertsson’s free surface

algorithm. This would allow the fine gridding to be restricted to the near-surface region, while coarser gridding could be used in other parts of the model.

Here, we show an alternative method to incorporate surface topography. An irregular-triangular-grid method is presented in Nolte *et al.* (1996) which is based on a finite-volume approximation (e.g., Vinokur, 1989) to the wave equation. This method allows the grid itself to be distorted so that grid points can be positioned directly on interfaces. Also, it deals with an irregular free surface the same way as with an irregular solid-solid interface, which is an advantage over the technique of Muir *et al.* (1992).

We demonstrate the usefulness of this method with numerical examples. First, we compare the irregular-grid technique for a model containing a sloping interface with a regular finite-difference code, and show that the former can model this case more accurately than the latter. We then present a numerical example that shows how the technique can be applied to a model with an irregular free surface. Finally, using a model of realistic surface topography, we show how the topography can effect regional seismograms.

## The Modeling Technique

We have described the modeling technique elsewhere

(Nolte *et al.*, 1996) and will thus only review the essentials. As there was an error in the P-SV formulation in the previous paper, we give the correct P-SV equations in the appendix. The method essentially amounts to a discrete approximation to the wave equation in integral form, while the constitutive relation is approximated in finite-difference form. The model is parameterized on

a triangular Delaunay grid and its dual Dirichlet grid (see the appendix and Figure A-2 for the definition of these terms). As the Delaunay grid can be irregular, grid points can be placed directly on an interface. In our irregular-grid technique the medium parameters ( $\lambda$ ,  $\mu$  and  $\rho$ ) are defined to be constant within each triangular grid cell (see Figure A-2). Thus, if grid points are positioned exactly on an interface, the two media will be separated exactly by the interface. In contrast, finite-difference implementations usually approximate the model parameters in an area around the grid point itself, which in staggered-grid techniques does not clearly define the exact position of an interface.

As stated above, the free surface is treated the same way as any other interface. On all other model boundaries, we use Higdon's (1986, 1987) absorbing boundary condition.

## Comparison With Finite Difference for a Dipping Interface

In order to test the performance of the irregular-grid code, we have designed the following experiment. First, we model a case of a flat interface (Figure 1a). For this type of model no stair-step approximation needs to be made, therefore a regular finite-difference technique should give accurate results. The depth to the interface is 800 m, and the source is located 120 m above the interface. The P and S velocities and densities of the two layers are given in the figure. A snapshot computed with finite differences for the model in Figure 1a is shown in Figure 2a. The snapshot shows the horizontal component of particle velocity (i.e., the component parallel to the interface) for a point-force source oriented vertically (perpendicular to the interface). The source signal is a Ricker wavelet with a center frequency of 20 Hz. The snapshot is taken at a time of 0.2 s. Next,

we rotate the whole experiment by  $30^\circ$  (Figure 1b), i.e., we rotate the interface, and the source orientation. The source is therefore still oriented perpendicular to the interface. For this model we now compute snapshots of the particle velocity component parallel to the interface. Thus, with the exception of the effects from the free surface and (imperfectly) absorbing boundaries, the snapshots computed for the tilted model should look like those computed for the flat model, but rotated by  $30^\circ$ . Figure 2b shows the result computed with the finite-difference scheme, while Figure 3b shows the irregular-grid result. In the irregular-grid computation, the grid has been distorted in such a way that particle-velocity grid points lie exactly on the dipping interfaces. Figure 3a is the same as Figure 2a. It is shown here again in order to facilitate the comparison.

Comparison of Figure 2b with Figure 2a shows that while the overall appearance of the snapshots is still similar, some noticeable differences are observed particularly in the region (marked by a circle) in Figure 2b where several waves (the direct S wave, the reflected S wave, and the P to S converted wave) interfere, and where a critical angle for the reflected S is present. The amplitude-versus-angle behavior of the waves reflected at the sloping interface is no longer modeled accurately. Comparison of Figure 3a with Figure 3b, on the other hand, shows that the accuracy of the amplitude-versus-angle behavior for the tilted interface has improved considerably. Figure 3b is more or less a tilted version of Figure 3a.

This comparison demonstrates that, as expected, the irregular-grid method can model irregular interfaces more accurately than a standard finite-difference scheme.

## A Simple Free-Surface Example

As the irregular-grid technique is able to handle irregular solid-solid interfaces, it can be applied with confidence to an irregular free surface. This is because, as mentioned above, the method treats the free surface the same way as any other interface. To demonstrate this capability, we now apply it to a model with irregular surface topography, where the grid is computed in such a way that it lines up with the surface.

First, Figure 4 shows an example of such a grid approximating a sloping surface. Note that only triangles with at least one of their vertices at the free surface are distorted. All other triangles are equilateral. For equilateral triangles our modeling scheme is of second-order accuracy. Otherwise the accuracy is first-order. For the gridding used in Figure 4 and in the example below the accuracy is therefore second-order everywhere, except on the free surface where it is first-order. Also note that the grid has been computed in such a way that none of the distorted triangles have angles greater than  $90^\circ$ . This is desirable, as it facilitates computation of the area elements  $A$  and the polygons  $\partial A$  (see the appendix for the definition of these terms). The reason for this is that for triangles with angles  $\leq 90^\circ$  the circumcenter (the center of the circle through the vertices, see Figure A-2) is located within that triangle. A triangle with an obtuse angle, on the other hand, would have its circumcircle outside the triangle, which can be easily visualized from Figure A-2.

A model with irregular surface topography is shown in Figure 5. The horizontal length of the model is 2 km, the average vertical length is 1.1 km. The topographic relief is 200 m. A single reflecting interface is located at an average depth of 800 m (300 m from the bottom). The P and S velocities and the density are given in the figure.

Figure 6 shows a series of snapshot taken at time intervals of 0.05 s, starting at a time of 0.1 s. In this case, the source was a vertically oriented point force, and the snapshots show the vertical component of particle velocity. The most prominent effect of the irregular surface topography is the presence of scattered surface waves, primarily from the peak at about one-third of the horizontal model length from the left. These scattered waves can be seen best at the later times. As can be seen, both incident P waves and S waves cause these scattered waves.

## Modeling Rough-Topography Effects on Regional Wave Propagation

We now use our modeling technique to study the effect of irregular surface topography on regional seismograms. The topography in our model (Figure 7a) is a realistic example of the topography that can be encountered along profiles in the Middle East. It was obtained with the online profile maker from *Cornell University's Middle East and North Africa Project* database (<http://atlas.geo.cornell.edu>) for a profile in northern Iran. Figure 7b shows the entire model used for our investigation. It consists of three layers with P and S velocities given in the figure.

We computed synthetic seismograms for this model with and without including the surface topography. We use a source signal with a center frequency of 0.6 Hz for this computation. The results are shown in Figure 8. There are some distinct differences in the waveforms obtained for the two cases. In this example, the most prominent differences are on the vertical component at larger arrival times (greater than 70 s). More arrivals with higher amplitudes are present in the case of surface topography. These arrivals are most likely due to surface waves that arise from body-wave

scattering at the rough surface, the same effect we observed in the irregular-surface example in the previous section.

Our comparison demonstrates that a pronounced surface topography, such as is present in many regions, e.g. the Middle East, will have a distinct effect on observed waveforms, and should thus be included in the modeling. Our newly developed method provides a valuable tool for this task.

## Discussion

The memory requirements of the technique have not been addressed thus far. The irregular grid requires more memory per grid point than a regular-grid method. The additional quantities that need to be stored for each grid point are its coordinates and the indices of its neighbors. Also, the total number of stress points will be larger than the total number of velocity points (the exact ratio of these two quantities depends on the grid irregularity). On the other hand, the method allows variable grid-point spacing, so that the spacing can be locally scaled to the medium velocity as well as to the amount of detail with which one desires to model particular areas of a model. For example, for a model in which regions with strongly different velocities are present, the irregular-grid method would require fewer grid points than a second-order finite-difference program and would thus allow the model size to be larger.

A potential extension of the code to 3-D is easy in principle. Taking the method to 3-D would require tetrahedral instead of triangular Delaunay cells. In practice, one of the main difficulties is the problem of the grid computation itself, i.e., fitting a tetrahedral grid to a model in such a way that it lines up with the interfaces and that the grid spacing is scaled to the medium velocities.

However, the development of efficient 3-D gridding algorithms is an area of extensive research (e.g., the GOCAD Research Program), so that existing software can be used to perform this task.

## Conclusions

In this study, we have demonstrated the ability of the irregular-grid technique to accurately model irregular interfaces. A comparison with a finite-difference technique showed that the irregular-grid method produced superior results, as no stair-step approximation to interfaces is made. We also showed the applicability of the method to an irregular free surface. A numerical test showed that surface irregularities gave rise to numerous scattered waves. We observed the same scattering effect in regional synthetics computed for a model with realistic surface topography.

## References

Alford, R. M., Kelly, K. R., and Boore, D. M., 1974, Accuracy of finite-difference modeling of the acoustic wave equation, *Geophysics*, *39*, 834–842.

Dirichlet, G. L., 1850, Über die Reduktion der positiven quadratischen Formen mit drei unbestimmten ganzen Zahlen, *J. Reine u. Angew. Math.*, *40*, 209–227.

Delaunay, B. N., 1934, Sur la sphere vide, *Bull. Acad. Science, USSR VII: Class. Sci. Math.*, 793–800.

De Lilla, A., 1997, Finite difference seismic wave propagation using variable grid sizes, *M.Sc. Thesis, Massachusetts Institute of Technology*.

Hestholm, S. O., 1996, 3-D finite-difference elastic wave modeling including surface topography, *66th Ann. Int. Mtg. Soc. Expl. Geophys., Expanded Abstracts*, 662–665.

Hestholm, S. O. and Ruud, B. O., 1994, 2-D finite-difference elastic wave modelling including surface topography, *Geophys. Prosp.*, *42*, 371–390.

Higdon, R. L., 1986, Absorbing boundary conditions for difference approximations to the multi-dimensional wave equation, *Math. Comp.*, *47*, 437–459.

Higdon, R. L., 1987, Numerical absorbing boundary conditions for the wave equation, *Math. Comp.*, *49*, 65–90.

Jastram, C. and Tessmer, E., 1994, Elastic modeling on a grid with vertically varying spacing, *Geophys. Prosp.*, *42*, 357–370.

Jih, R. S., McLaughlin, K. R., and Der, Z. A., 1988, Free-boundary conditions of arbitrary polygonal topography in a two-dimensional explicit elastic finite-difference scheme, *Geophysics*, *53*, 1045–

1055.

Levander, A. R., 1988, Fourth-order finite-difference P-SV seismograms, *Geophysics*, *53*, 1425–1436.

Muir, F., Dellinger, J., Etgen, J., and Nichols, D., 1992, Modeling elastic wave fields across irregular boundaries, *Geophysics* *57*, 1189–1193.

Nolte, B., Gibson, R. L., and Toksöz, M. N., 1996, Irregular-grid modeling of regional wave propagation, in J. Lewkowitz, J. M. McPhetres, and D. T. Reiter, editors, *Proceedings of the 18th Annual Seismic Research Symposium on Monitoring a Comprehensive Test Ban Treaty*, PL-TR-96-2153, pages 231–240, Hanscom AFB, MA. Phillips Laboratory, ADA313692.

Robertsson, J. O. A., 1996 A numerical free-surface condition for elastic/viscoelastic finite-difference modeling in the presence of topography, *66th Ann. Int. Mtg. Soc. Expl. Geophys., Expanded Abstracts*, 670–673.

Robertsson, J. O. A., Levander, A., Symes, W. W., and Hollinger, K., 1995, A comparative study of free-surface boundary conditions for finite-difference simulation of elastic/viscoelastic wave propagation, *65th Ann. Int. Mtg. Soc. Expl. Geophys., Expanded Abstracts*, 1277–1280.

Tessmer, E., Kosloff, D., and Behle, A., 1992, Elastic wave propagation simulation in the presence of surface topography, *Geophys. J. Int.*, *108*, 621–632.

Vinokur, M., 1989, An analysis of finite-difference and finite-volume formulations of conservation laws, *J. Comp. Phys.*, *81*, 1–52.

Virieux, J., 1984, SH wave propagation in heterogeneous media: velocity-stress finite-difference method, *Geophysics*, *49*, 1933–1957.

Virieux, J., 1986, P-SV wave propagation in heterogeneous media: velocity-stress finite-difference

method, *Geophysics*, 51, 889–901.

Wang, Y. and Schuster, G. T., 1996, Finite-difference variable grid scheme for acoustic and elastic wave equation modeling, *66th Ann. Int. Mtg. Soc. Expl. Geophys., Expanded Abstracts*, 674–677.

## Appendix

A more detailed description of the modeling technique is given in Nolte *et al.* (1996). Here, we only give a brief review of the method for the P-SV case and correct some errors of the earlier paper.

Figure A-1 defines some terms used in the equations below. For an area  $A$  with boundary  $\partial A$ , we introduce local coordinates  $n$  and  $s$ , normal and tangential to  $\partial A$ , respectively. With  $\phi$  denoting the angle between  $n$  and the Cartesian  $x$  direction, the local and Cartesian coordinates are related through:

$$\begin{aligned} n &= x \cos \phi + z \sin \phi \\ s &= -x \sin \phi + z \cos \phi \\ x &= n \cos \phi - s \sin \phi \\ z &= n \sin \phi + s \cos \phi \end{aligned} \tag{1}$$

Using the above definitions we write the wave equation in integral form as

$$\begin{aligned} \iint_A dA \rho \frac{\partial v_x}{\partial t} &= \oint_{\partial A} ds (\sigma_{nn} \cos \phi - \sigma_{ns} \sin \phi) \\ \iint_A dA \rho \frac{\partial v_z}{\partial t} &= \oint_{\partial A} ds (\sigma_{nn} \sin \phi + \sigma_{ns} \cos \phi). \end{aligned} \tag{2}$$

Here,  $v_x$  and  $v_z$  are the  $x$  and  $z$  components, respectively, of the particle velocity, while  $\sigma_{nn}$  and  $\sigma_{ns}$  are the normal and tangential stresses on  $\partial A$ .

The constitutive relation (Hooke's law) can be written as

$$\begin{aligned} \frac{\partial \sigma_{nn}}{\partial t} &= (\lambda + 2\mu) \left( \frac{\partial v_x}{\partial n} \cos \phi + \frac{\partial v_z}{\partial n} \sin \phi \right) + \lambda \left( \frac{\partial v_z}{\partial s} \cos \phi - \frac{\partial v_x}{\partial s} \sin \phi \right) \\ \frac{\partial \sigma_{ns}}{\partial t} &= \mu \left[ \left( \frac{\partial v_z}{\partial n} + \frac{\partial v_x}{\partial s} \right) \cos \phi + \left( \frac{\partial v_z}{\partial s} - \frac{\partial v_x}{\partial n} \right) \sin \phi \right]. \end{aligned} \tag{3}$$

In order to discretize these equations, the model is parameterized using Delaunay and Dirichlet grids (Delaunay, 1934; Dirichlet, 1850) as illustrated in Figure A-2. A Delaunay grid is a triangular grid that connects nearest neighbors. This nearest-neighbor condition means that a circle through the three vertices of any triangle (a so-called *circumcircle*) does not enclose any other vertex. The corresponding Dirichlet grid is obtained by connecting the centers of the circumcircles (the *circumcenters*) of neighboring Delaunay triangles.

We now specify particle velocity at the Delaunay vertices, and use the area enclosed by the polygon around any particle-velocity point as the area  $A$  of Figure A-1 while we use the polygon itself as its boundary  $\partial A$ . We assume that the medium parameters ( $\lambda$ ,  $\mu$ , and  $\rho$ ) as well as all stresses are constant within each Delaunay triangle.

The notations used are shown in Figure A-3a and A-3b. In Figure A-3b, we have introduced the velocities  $v_1, v_2, v_3$ , and  $v_4$ , for convenience. As can be seen,  $v_3$  is the velocity  $v_{[j,k-1]}$ , and  $v_2$  is  $v_{[j,k+1]}$ ;  $v_1$  is interpolated from  $v_j$ ,  $v_{[j,k]}$ , and  $v_2$ ;  $v_4$  is interpolated from  $v_j$ ,  $v_3$ , and  $v_{[j,k]}$ . Denoting the time index by  $m$  we obtain the discrete form of the wave equation as

$$\begin{aligned} v_x^m_{[j]} &= v_x^{m-1}_{[j]} + \left( \frac{\Delta t}{\sum_{k=1}^{N_k} A_{[j,k]} \rho_{[j,k]}} \right) \sum_{k=1}^{N_k} (l_{[j,k]}^+ [\sigma_{nn}^{+[m-1/2]} \cos \phi - \sigma_{ns}^{+[m-1/2]} \sin \phi] \\ &\quad + l_{[j,k]}^- [\sigma_{nn}^{-[m-1/2]} \cos \phi - \sigma_{ns}^{-[m-1/2]} \sin \phi]) \\ v_z^m_{[j]} &= v_z^{m-1}_{[j]} + \left( \frac{\Delta t}{\sum_{k=1}^{N_k} A_{[j,k]} \rho_{[j,k]}} \right) \sum_{k=1}^{N_k} (l_{[j,k]}^+ [\sigma_{nn}^{+[m-1/2]} \sin \phi + \sigma_{ns}^{+[m-1/2]} \cos \phi] \\ &\quad + l_{[j,k]}^- [\sigma_{nn}^{-[m-1/2]} \sin \phi + \sigma_{ns}^{-[m-1/2]} \cos \phi]). \end{aligned} \quad (4)$$

We obtain the discrete form of the constitutive relation as

$$\begin{aligned}
\sigma_{nn}^{+[m+1/2]} &= \sigma_{nn}^{[m-1/2]} + \frac{\Delta t}{d_{[j,k]}}(\lambda^+ + 2\mu^+)(\Delta v_n)_{[j,k]} + \lambda^+ \frac{\Delta t}{e_{[j,k]}^+} (\Delta v_s)_{[j,k]}^+ \\
\sigma_{nn}^{-[m+1/2]} &= \sigma_{nn}^{-[m-1/2]} + \frac{\Delta t}{d_{[j,k]}}(\lambda^- + 2\mu^-)(\Delta v_n)_{[j,k]} + \lambda^- + \frac{\Delta t}{e_{[j,k]}^-} (\Delta v_s)_{[j,k]}^- \\
\sigma_{ns}^{+[m+1/2]} &= \sigma_{ns}^{[m-1/2]} + \frac{\Delta t}{d_{[j,k]}}\mu^+(\Delta v_s)_{[j,k]} + \frac{\Delta t}{e_{[j,k]}^+}\mu^+(\Delta v_n)_{[j,k]}^+ \\
\sigma_{ns}^{-[m+1/2]} &= \sigma_{ns}^{-[m-1/2]} + \frac{\Delta t}{d_{[j,k]}}\mu^-(\Delta v_s)_{[j,k]} + \frac{\Delta t}{e_{[j,k]}^-}\mu^-(\Delta v_n)_{[j,k]}^-.
\end{aligned} \tag{5}$$

The indices  $+$  and  $-$  refer to the two different grid cells, respectively, bordering on the line from point  $j$  to neighbor  $k$  (see Figure A-3b). In Eq. (5) we have used the following abbreviations for the normal velocity derivatives

$$\begin{aligned}
\Delta v_n &= (v_{xk}^m - v_{xj}^m) \cos \phi + (v_{zk}^m - v_{zj}^m) \sin \phi] \\
\Delta v_s &= -(v_{xk}^m - v_{xj}^m) \sin \phi + (v_{zk}^m - v_{zj}^m) \cos \phi].
\end{aligned} \tag{6}$$

and for tangential velocity derivatives (see Figure A-2b)

$$\begin{aligned}
(\Delta v_n)^+ &= (v_{x2}^m - v_{x1}^m) \cos \phi + (v_{z2}^m - v_{z1}^m) \sin \phi] \\
(\Delta v_n)^- &= (v_{x4}^m - v_{x3}^m) \cos \phi + (v_{z4}^m - v_{z3}^m) \sin \phi] \\
(\Delta v_s)^+ &= -(v_{x2}^m - v_{x1}^m) \sin \phi + (v_{z2}^m - v_{z1}^m) \cos \phi] \\
(\Delta v_s)^- &= -(v_{x4}^m - v_{x3}^m) \sin \phi + (v_{z4}^m - v_{z3}^m) \cos \phi].
\end{aligned} \tag{7}$$

As can be seen in the above equations the particle velocities are updated at time steps  $m = 1, 2, \dots$  whereas stresses are updated at time steps  $m = 1/2, 3/2, \dots$  analogously to a staggered-grid finite-difference approach.

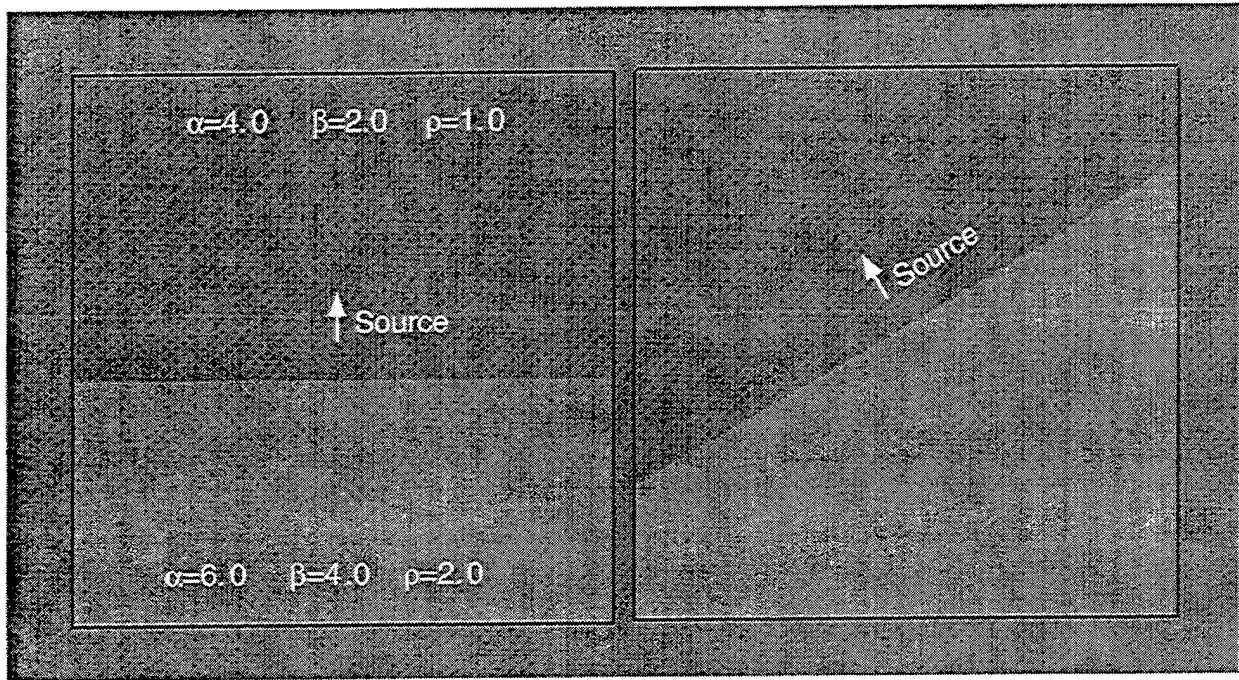


Figure 1: Models used for comparing the irregular-grid method with finite differences. The P and S velocities (in  $\text{km s}^{-1}$ ) and densities (in  $\text{g cm}^{-3}$ ) are given in the figure. (a) A flat interface is located at a depth of 800 m. The source is a point force located 120 m above the interface. The source orientation is perpendicular to the interface as indicated by an arrow in the figure. (b) The experiment is rotated by  $30^\circ$ . The source orientation is again indicated by an arrow in the picture.

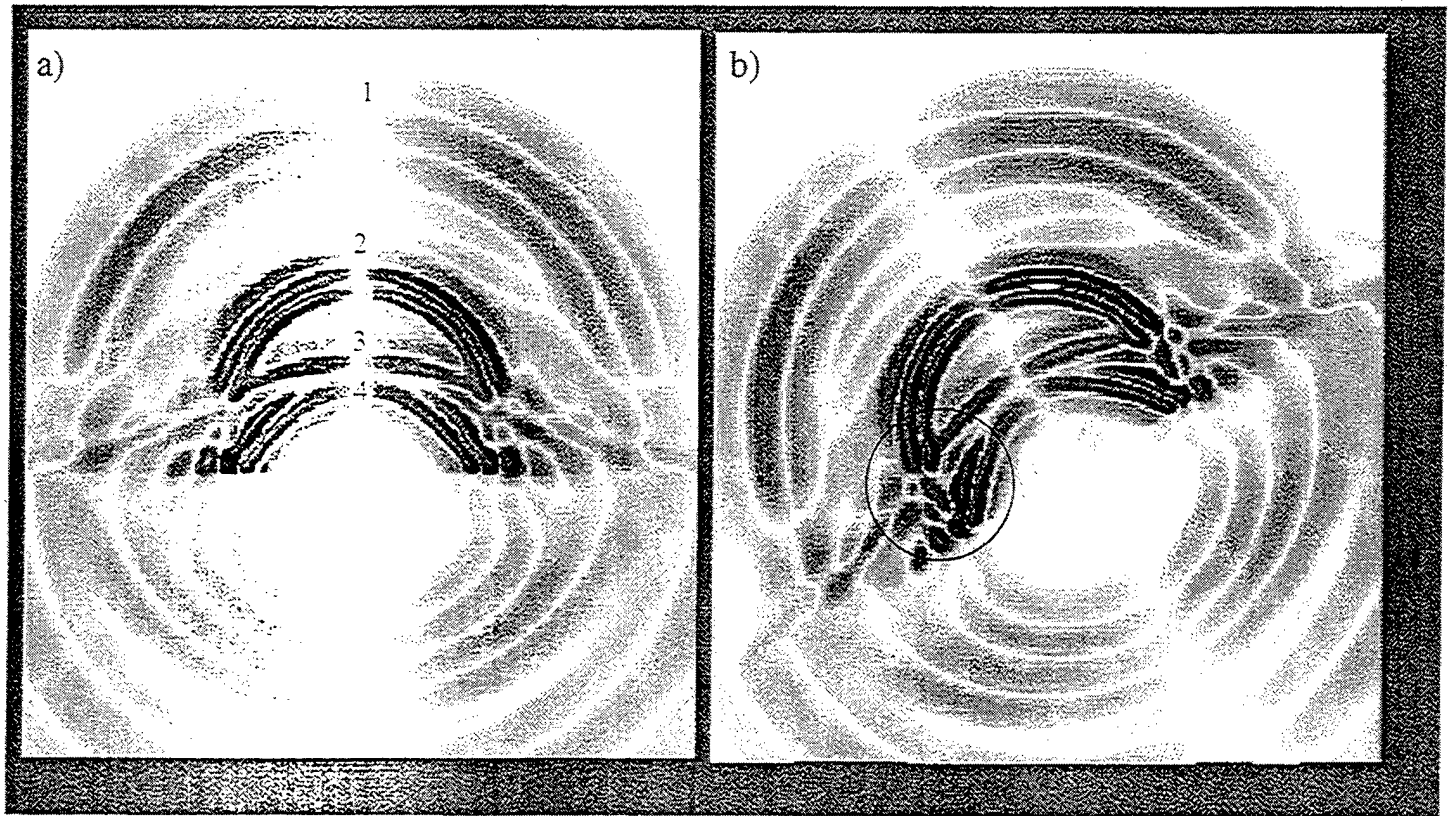


Figure 2: Snapshots computed with finite differences for (a) the model of Figure 1a and (b) the model of Figure 1b. The snapshots show the component of particle velocity parallel to the interface at the time of 0.2 s. The waves identified in (a) are the direct P wave (1), the direct S wave (2), the P-to-S converted wave (3), and the reflected S wave (4). The region enclosed by the circle in (b) is inaccurately modeled with finite differences.

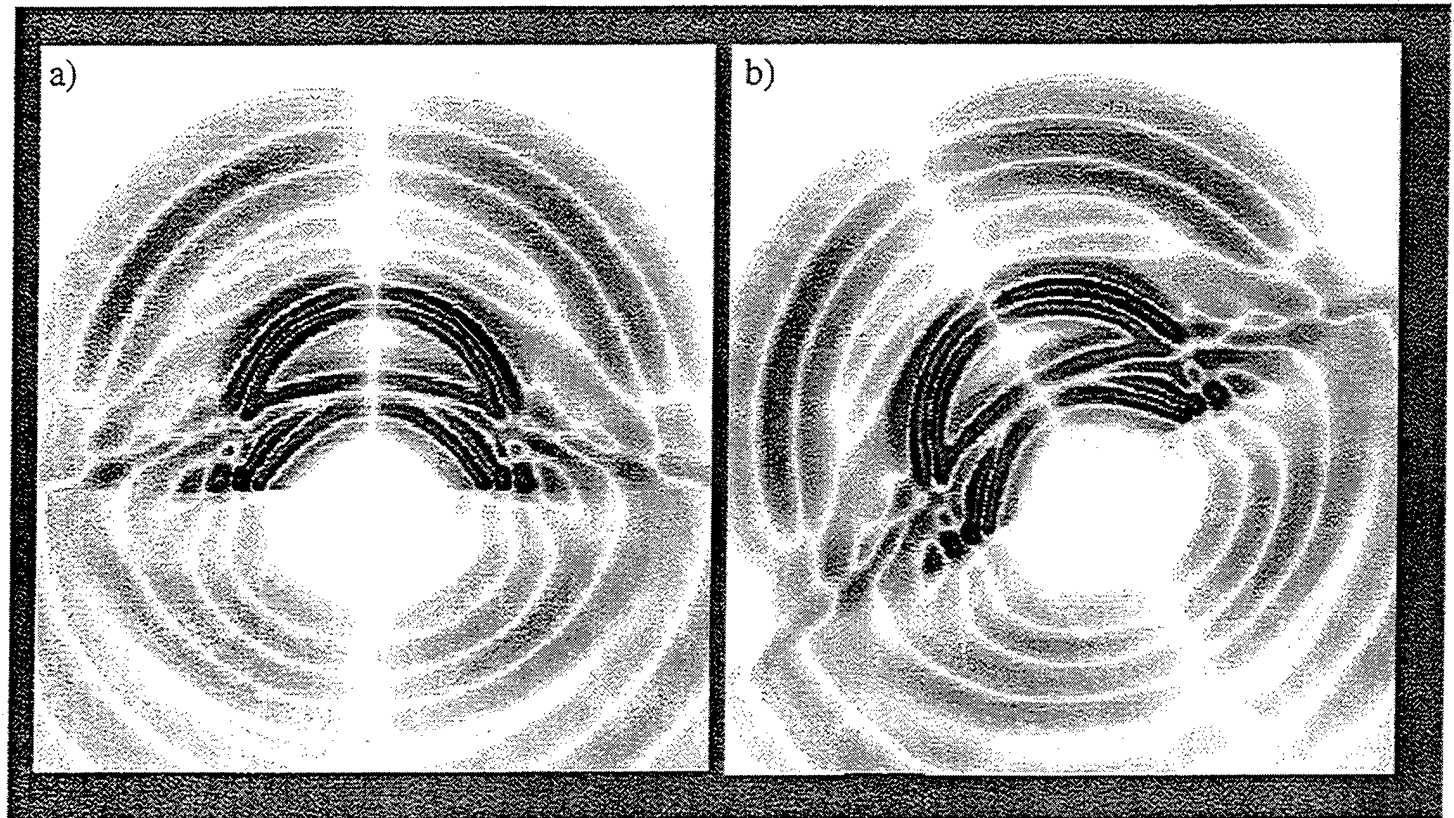


Figure 3: Same as Figure 2, but showing the snapshot computed with the irregular-grid method (b) for the tilted-interface model. Note the improved accuracy, particularly in the region where the finite-differences results were inaccurate (the region circled in Figure 2b).

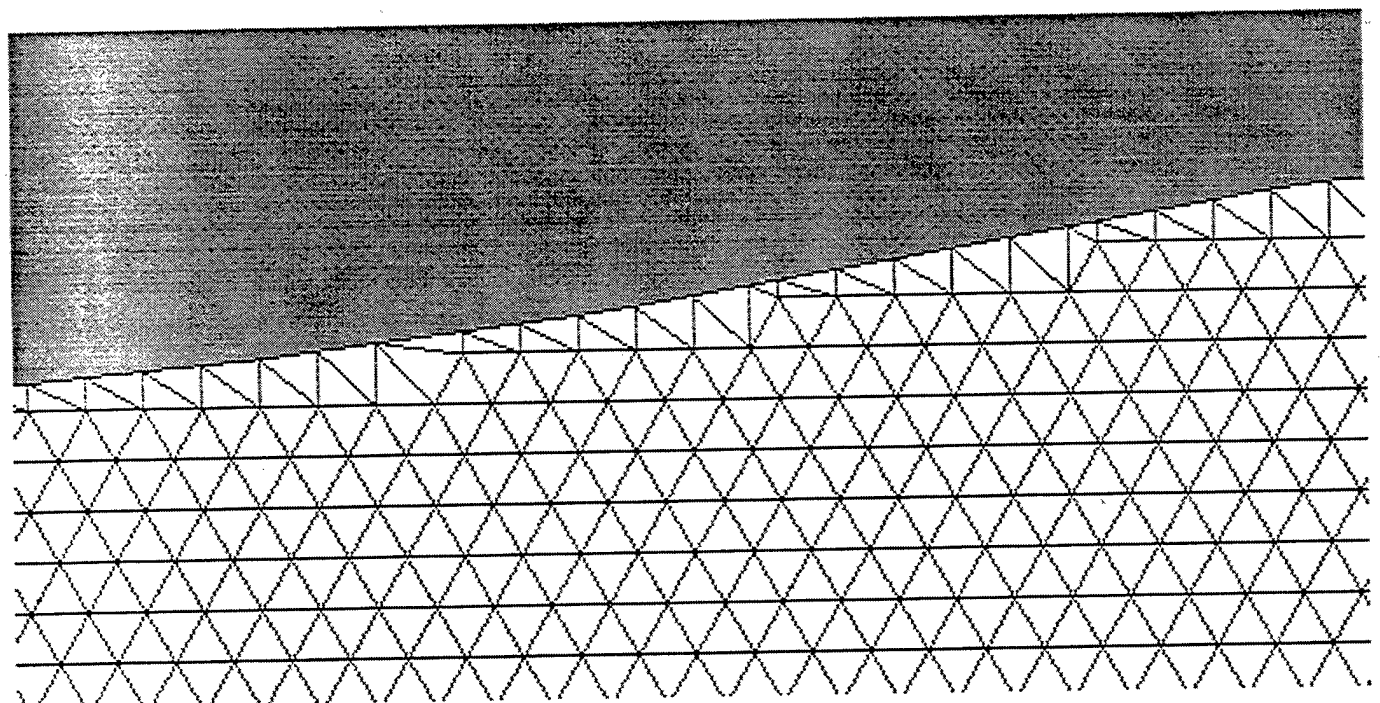


Figure 4: Example of a triangular grid that is lined up with an irregular free surface. All triangles except those that touch the free surface are equilateral. No angles greater than  $90^\circ$  are present anywhere in the grid.

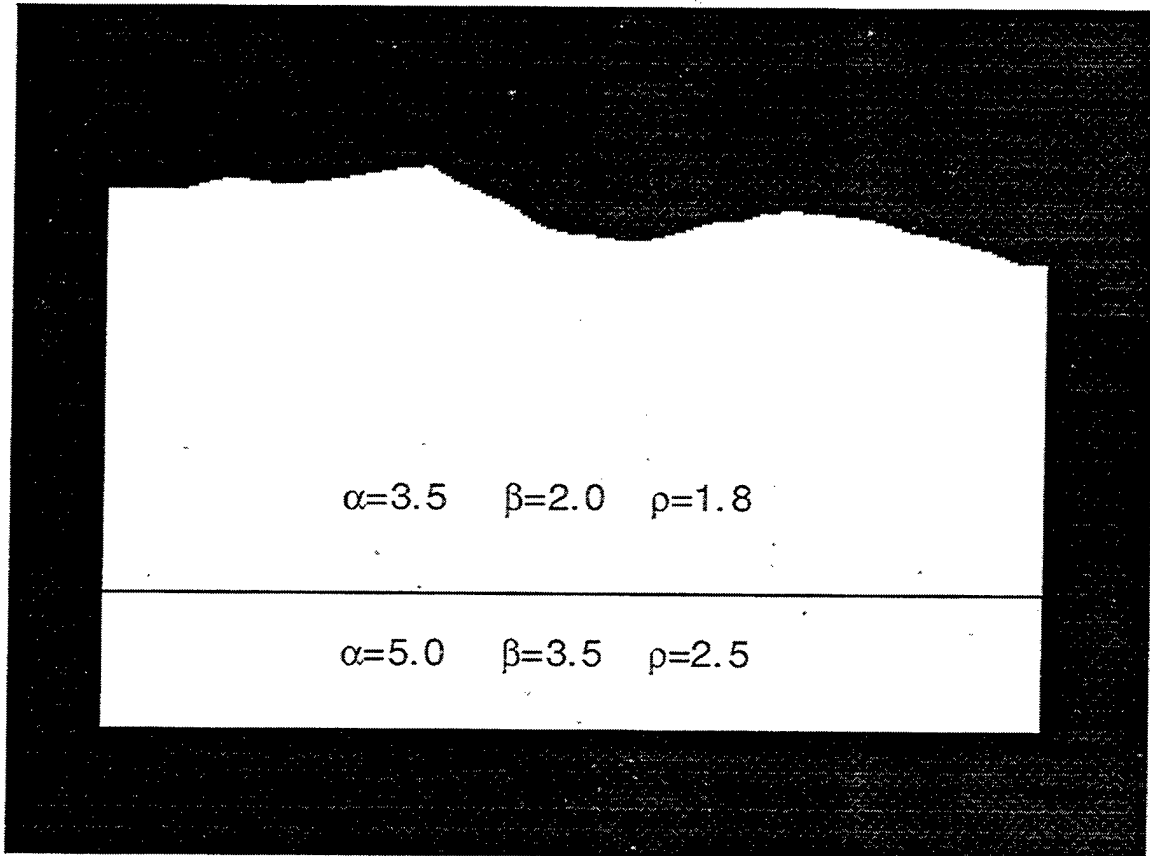


Figure 5: Model with irregular topography. The P and S velocities (in  $\text{km s}^{-1}$ ) and densities (in  $\text{g cm}^{-3}$ ) are given in the figure. The length of the model is 2 km, its height varies between 1 km and 1.2 km. This model is the input for the snapshots of Figure 6.

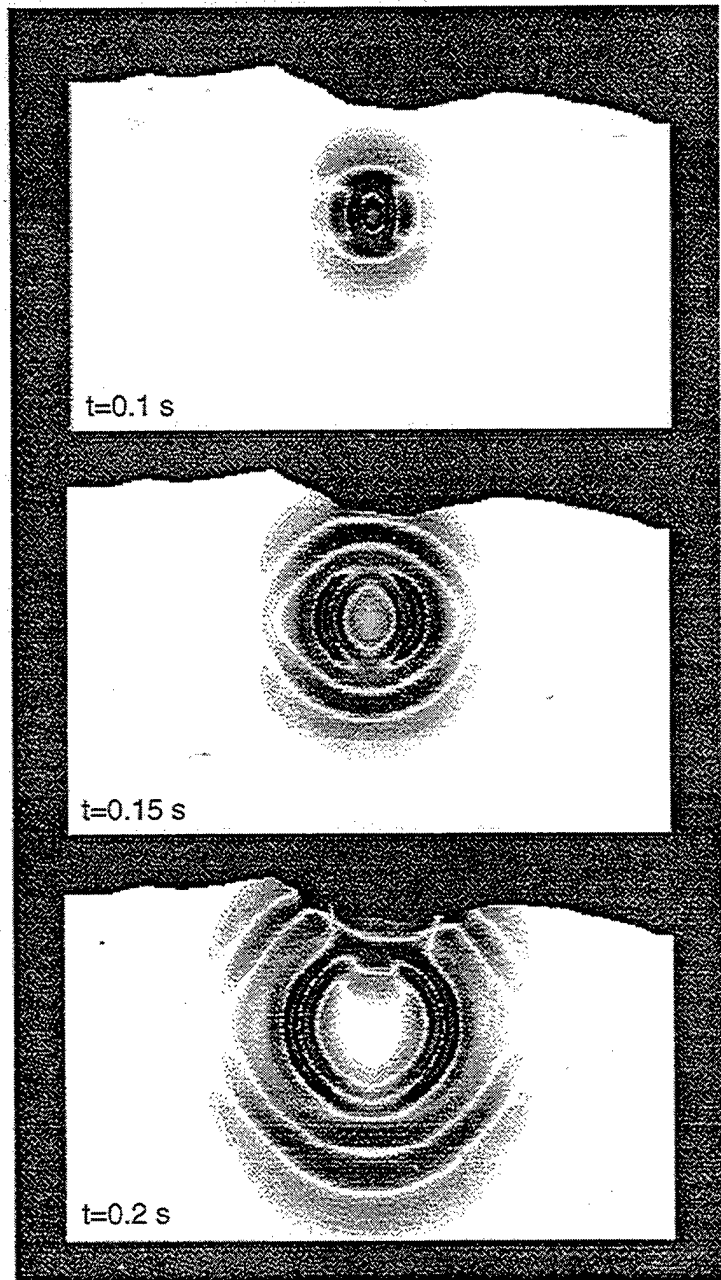


Figure 6: Snapshots computed for the model in Figure 5. The snapshots show the vertical component of particle velocity for at time intervals of 0.05 s, starting at 0.1 s. The source is a vertical point force.

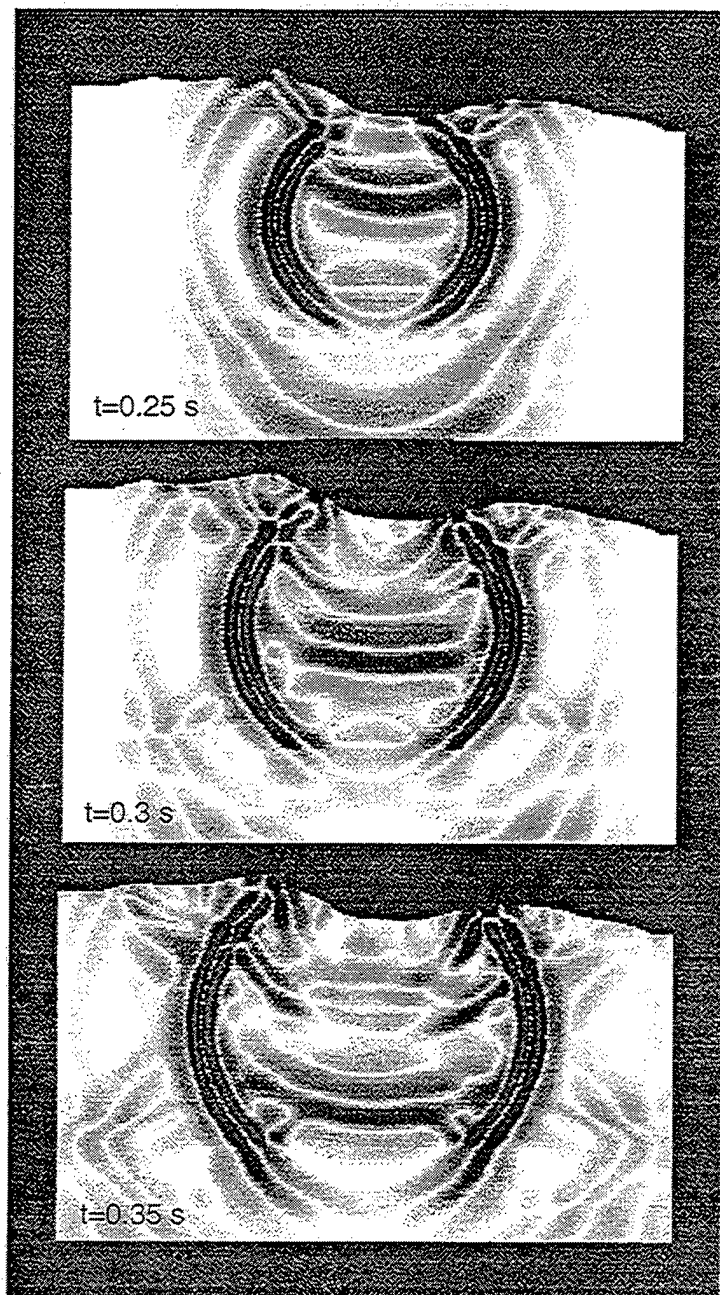


Figure 6, continued:

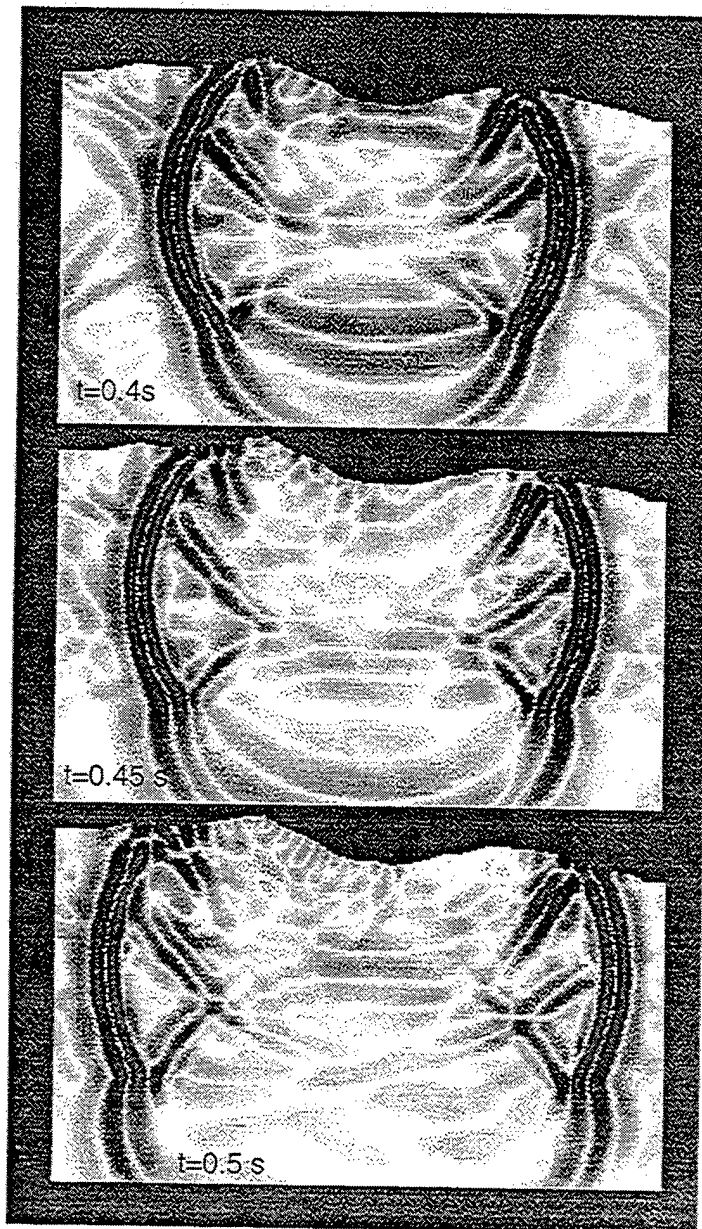


Figure 6, continued:

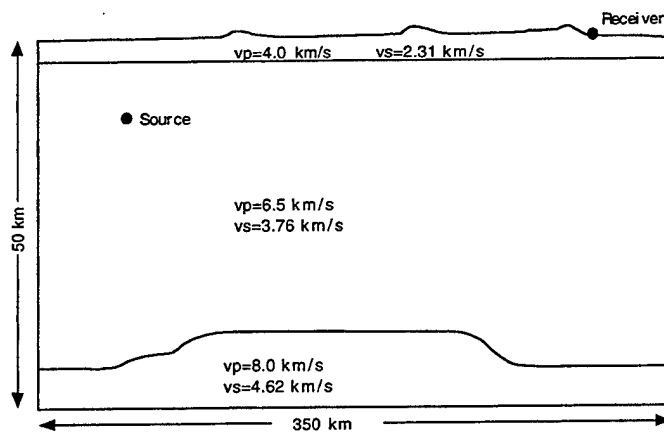
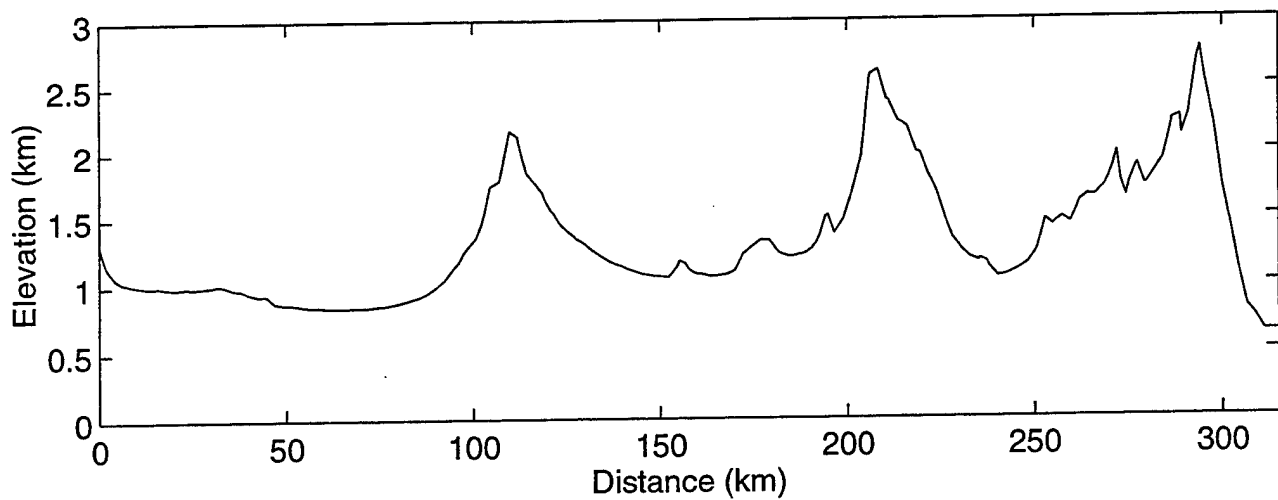


Figure 7: Irregular surface topography (a) and three-layer model (b) for regional wave propagation simulation. The source-receiver offset is 259 km. The source depth is 10 km.

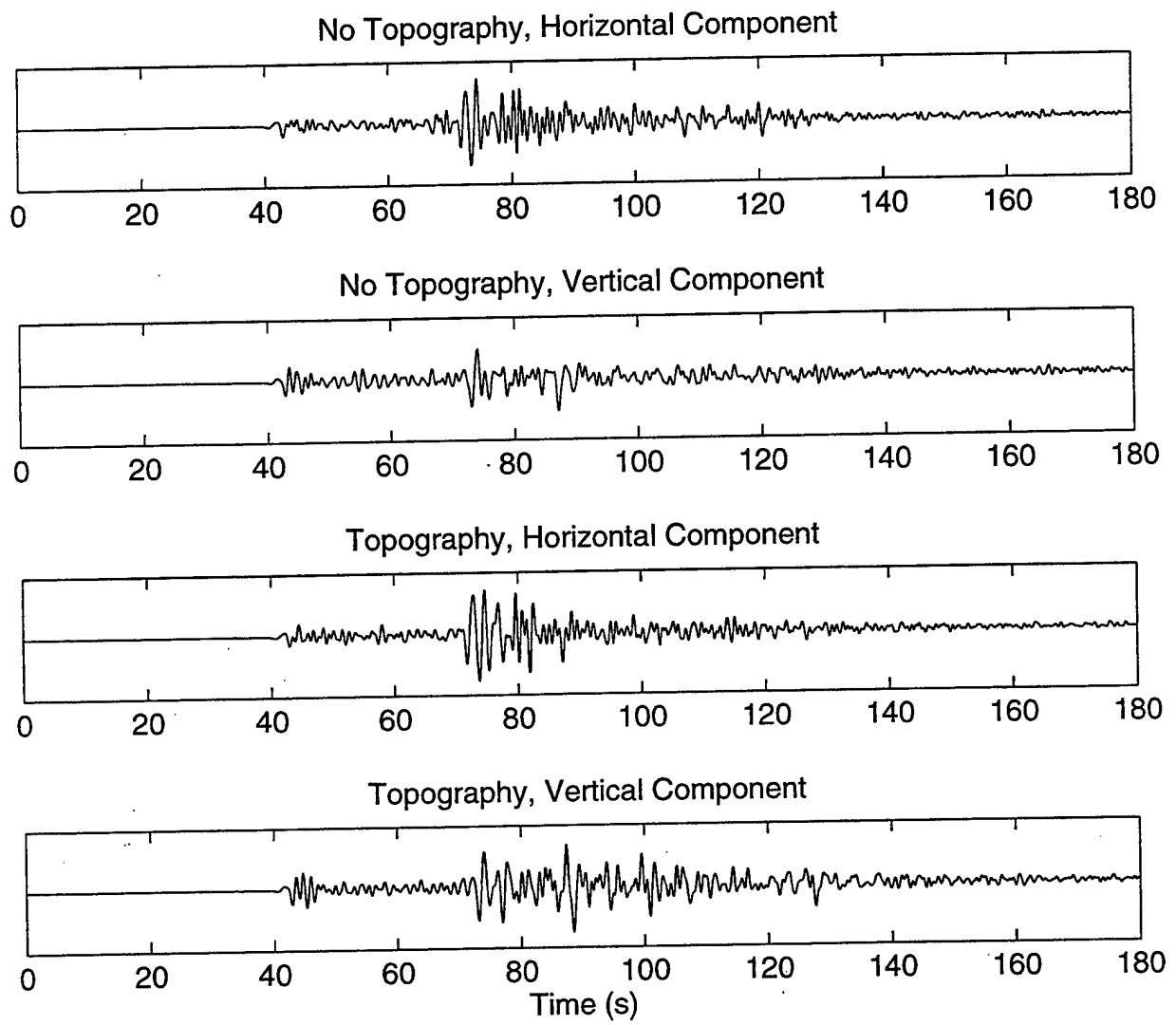


Figure 8: Synthetic waveforms computed for the model in Figure 7 with and without accounting for surface topography.

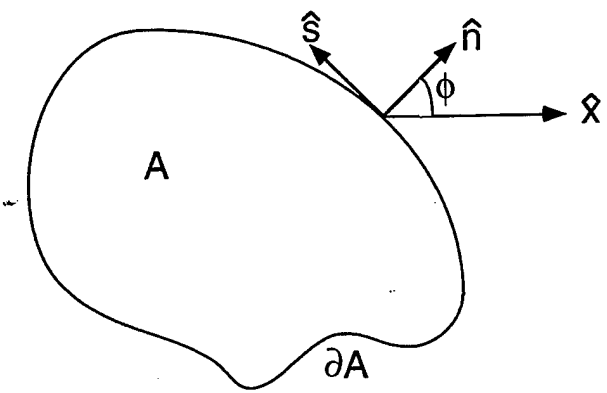


Figure A-1: Definition of the area  $A$ , its boundary  $\partial A$ , the local coordinates  $n$  and  $s$ , and the angle  $\phi$  used in the equations in the appendix.

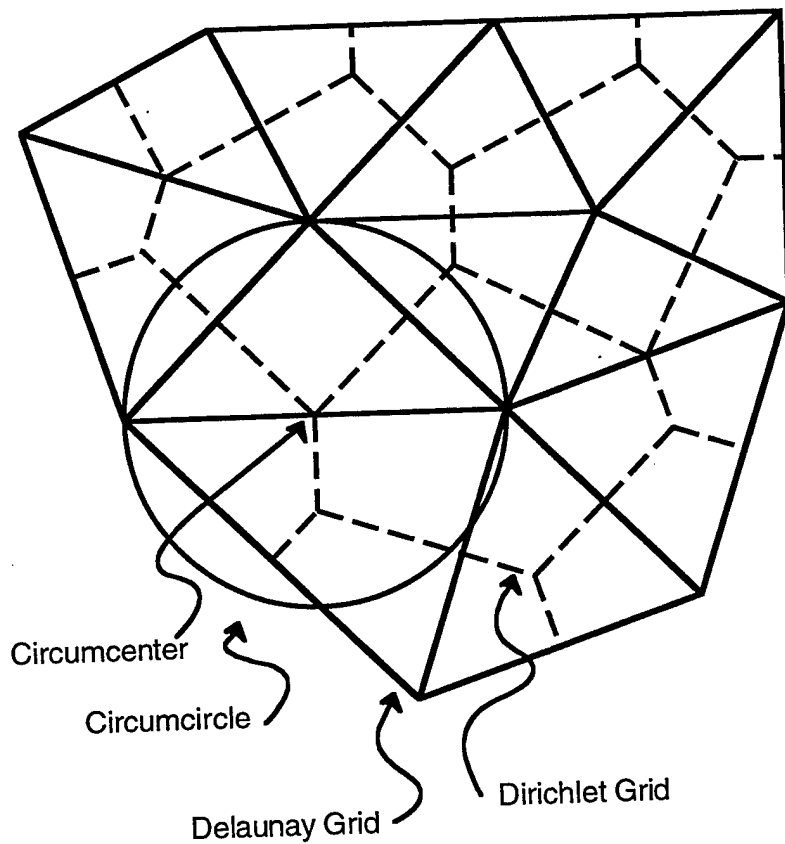


Figure A-2: Schematic of a Delaunay grid and its dual Dirichlet grid. The circumcircle through the vertices of any Delaunay triangle does not contain any other triangle vertices. The circumcenters are the vertices of the Dirichlet grid.

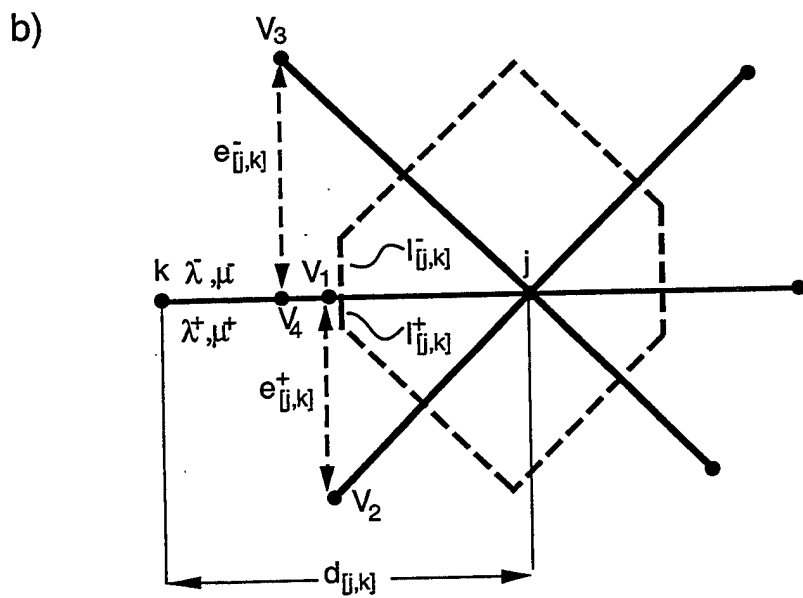
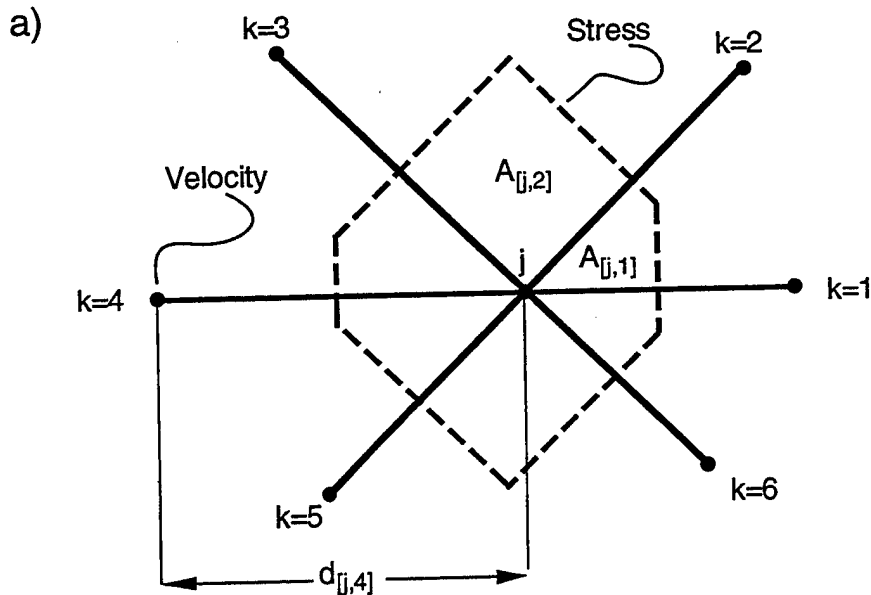


Figure A-3: Sketch of the terms used in the discrete equations. (a) A particle-velocity point  $j$  with six neighbors  $k$  is shown. Stress is integrated over the dashed polygon.  $A_{[j,k]}$  is an area element, and  $d_{[j,k]}$  is the distance from point  $j$  to neighbor  $k$ . (b) Line segments  $l_{[j,k]}$  over which stress is summed; velocity points  $v_1, v_2, v_3$ , and  $v_4$  and lengths  $e_{[j,k]}$  used for the computation of tangential velocity differences.

THOMAS AHRENS  
SEISMOLOGICAL LABORATORY 252-21  
CALIFORNIA INSTITUTE OF TECHNOLOGY  
PASADENA, CA 91125

AIR FORCE RESEARCH LABORATORY  
ATTN: VSOE  
29 RANDOLPH ROAD  
HANSCOM AFB, MA 01731-3010 (2 COPIES)

AIR FORCE RESEARCH LABORATORY  
ATTN: RESEARCH LIBRARY/TL  
5 WRIGHT STREET  
HANSCOM AFB, MA 01731-3004

AIR FORCE RESEARCH LABORATORY  
ATTN: AFRL/SUL  
3550 ABERDEEN AVE SE  
KIRTLAND AFB, NM 87117-5776 (2 COPIES)

RALPH ALEWINE  
NTPO  
1901 N. MOORE STREET, SUITE 609  
ARLINGTON, VA 22209

MUAWIA BARAZANGI  
INSTITUTE FOR THE STUDY OF THE CONTINENTS  
3126 SNEE HALL  
CORNELL UNIVERSITY  
ITHACA, NY 14853

T.G. BARKER  
MAXWELL TECHNOLOGIES  
8888 BALBOA AVE.  
SAN DIEGO, CA 92123-1506

DOUGLAS BAUMGARDT  
ENSCO INC.  
5400 PORT ROYAL ROAD  
SPRINGFIELD, VA 22151

THERON J. BENNETT  
MAXWELL TECHNOLOGIES  
11800 SUNRISE VALLEY DRIVE SUITE 1212  
RESTON, VA 22091

WILLIAM BENSON  
NAS/COS  
ROOM HA372  
2001 WISCONSIN AVE. NW  
WASHINGTON DC 20007

JONATHAN BERGER  
UNIVERSITY OF CA, SAN DIEGO  
SCRIPPS INSTITUTION OF OCEANOGRAPHY IGPP, 0225  
9500 GILMAN DRIVE  
LA JOLLA, CA 92093-0225

ROBERT BLANDFORD  
AFTAC  
1300 N. 17TH STREET  
SUITE 1450  
ARLINGTON, VA 22209-2308

LESLIE A. CASEY  
DEPT. OF ENERGY/NN-20  
1000 INDEPENDENCE AVE. SW  
WASHINGTON DC 20585-0420

CENTER FOR MONITORING RESEARCH  
ATTN: LIBRARIAN  
1300 N. 17th STREET, SUITE 1450  
ARLINGTON, VA 22209

ANTON DAINTY  
HQ DSWA/PMP  
6801 TELEGRAPH ROAD  
ALEXANDRIA, VA 22310-3398

CATHERINE DE GROOT-HEDLIN  
UNIVERSITY OF CALIFORNIA, SAN DIEGO  
INSTITUTE OF GEOPHYSICS AND PLANETARY PHYSICS  
8604 LA JOLLA SHORES DRIVE  
SAN DIEGO, CA 92093

DEFENSE TECHNICAL INFORMATION CENTER  
8725 JOHN J. KINGMAN ROAD  
FT BELVOIR, VA 22060-6218 (2 COPIES)

DIANE DOSER  
DEPARTMENT OF GEOLOGICAL SCIENCES  
THE UNIVERSITY OF TEXAS AT EL PASO  
EL PASO, TX 79968

MARK D. FISK  
MISSION RESEARCH CORPORATION  
735 STATE STREET  
P.O. DRAWER 719  
SANTA BARBARA, CA 93102-0719

LORI GRANT  
MULTIMAX, INC.  
311C FOREST AVE. SUITE 3  
PACIFIC GROVE, CA 93950

HENRY GRAY  
SMU STATISTICS DEPARTMENT  
P.O. BOX 750302  
DALLAS, TX 75275-0302

I. N. GUPTA  
MULTIMAX, INC.  
1441 MCCORMICK DRIVE  
LARGO, MD 20774

DAVID HARKRIDER  
BOSTON COLLEGE  
INSTITUTE FOR SPACE RESEARCH  
140 COMMONWEALTH AVENUE  
CHESTNUT HILL, MA 02167

MICHAEL HEDLIN  
UNIVERSITY OF CALIFORNIA, SAN DIEGO  
SCRIPPS INSTITUTION OF OCEANOGRAPHY IGPP, 0225  
9500 GILMAN DRIVE  
LA JOLLA, CA 92093-0225

EUGENE HERRIN  
SOUTHERN METHODIST UNIVERSITY  
DEPARTMENT OF GEOLOGICAL SCIENCES  
DALLAS, TX 75275-0395

VINDELL HSU  
HQ/AFTAC/TTR  
1030 S. HIGHWAY A1A  
PATRICK AFB, FL 32925-3002

THOMAS JORDAN  
MASSACHUSETTS INSTITUTE OF TECHNOLOGY  
EARTH, ATMOSPHERIC & PLANETARY SCIENCES  
77 MASSACHUSETTS AVENUE, 54-918  
CAMBRIDGE, MA 02139

LAWRENCE LIVERMORE NATIONAL LABORATORY  
ATTN: TECHNICAL STAFF (PLS ROUTE)  
PO BOX 808, MS L-208  
LIVERMORE, CA 94551

LAWRENCE LIVERMORE NATIONAL LABORATORY  
ATTN: TECHNICAL STAFF (PLS ROUTE)  
PO BOX 808, MS L-195  
LIVERMORE, CA 94551

LAWRENCE LIVERMORE NAT'L LABORATORY  
ATTN: TECHNICAL STAFF (PLS ROUTE)  
PO BOX 808, MS L-200  
LIVERMORE, CA 94551

THORNE LAY  
UNIVERSITY OF CALIFORNIA, SANTA CRUZ  
EARTH SCIENCES DEPARTMENT  
EARTH & MARINE SCIENCE BUILDING  
SANTA CRUZ, CA 95064

THOMAS HEARN  
NEW MEXICO STATE UNIVERSITY  
DEPARTMENT OF PHYSICS  
LAS CRUCES, NM 88003

DONALD HELMBERGER  
CALIFORNIA INSTITUTE OF TECHNOLOGY  
DIVISION OF GEOLOGICAL & PLANETARY SCIENCES  
SEISMOLOGICAL LABORATORY  
PASADENA, CA 91125

ROBERT HERRMANN  
ST. LOUIS UNIVERSITY  
DEPARTMENT OF EARTH & ATMOSPHERIC SCIENCES  
3507 LACLEDE AVENUE  
ST. LOUIS, MO 63103

RONG-SONG JIH  
HQ DSWA/PMP/CTBT  
6801 TELEGRAPH ROAD  
ALEXANDRIA, VA 22310-3398

LAWRENCE LIVERMORE NATIONAL LABORATORY  
ATTN: TECHNICAL STAFF (PLS ROUTE)  
PO BOX 808, MS L-175  
LIVERMORE, CA 94551

LAWRENCE LIVERMORE NATIONAL LABORATORY  
ATTN: TECHNICAL STAFF (PLS ROUTE)  
PO BOX 808, MS L-202  
LIVERMORE, CA 94551

LAWRENCE LIVERMORE NATIONAL LABORATORY  
ATTN: TECHNICAL STAFF (PLS ROUTE)  
PO BOX 808, MS L-205  
LIVERMORE, CA 94551

LAWRENCE LIVERMORE NAT'L LABORATORY  
ATTN: TECHNICAL STAFF (PLS ROUTE)  
PO BOX 808, MS L-221  
LIVERMORE, CA 94551

ANATOLI L. LEVSHIN  
DEPARTMENT OF PHYSICS  
UNIVERSITY OF COLORADO  
CAMPUS BOX 390  
BOULDER, CO 80309-0309

JAMES LEWKOWICZ  
WESTON GEOPHYSICAL CORP.  
325 WEST MAIN STREET  
NORTHBORO, MA 01532

LOS ALAMOS NATIONAL LABORATORY  
ATTN: TECHNICAL STAFF (PLS ROUTE)  
PO BOX 1663, MS F659  
LOS ALAMOS, NM 87545

LOS ALAMOS NATIONAL LABORATORY  
ATTN: TECHNICAL STAFF (PLS ROUTE)  
PO BOX 1663, MS F665  
LOS ALAMOS, NM 87545

LOS ALAMOS NATIONAL LABORATORY  
ATTN: TECHNICAL STAFF (PLS ROUTE)  
PO BOX 1663, MS D460  
LOS ALAMOS, NM 87545

LOS ALAMOS NATIONAL LABORATORY  
ATTN: TECHNICAL STAFF (PLS ROUTE)  
PO BOX 1663, MS C335  
LOS ALAMOS, NM 87545

GARY MCCARTOR  
SOUTHERN METHODIST UNIVERSITY  
DEPARTMENT OF PHYSICS  
DALLAS, TX 75275-0395

KEITH MCLAUGHLIN  
CENTER FOR MONITORING RESEARCH (SAIC)  
1300 N. 17TH STREET, SUITE 1450  
ARLINGTON, VA 22209

BRIAN MITCHELL  
DEPARTMENT OF EARTH & ATMOSPHERIC SCIENCES  
ST. LOUIS UNIVERSITY  
3507 LACLEDE AVENUE  
ST. LOUIS, MO 63103

RICHARD MORROW  
USACDA/IVI  
320 21ST STREET, N.W.  
WASHINGTON DC 20451

JOHN MURPHY  
MAXWELL TECHNOLOGIES  
11800 SUNRISE VALLEY DRIVE SUITE 1212  
RESTON, VA 22091

JAMES NI  
NEW MEXICO STATE UNIVERSITY  
DEPARTMENT OF PHYSICS  
LAS CRUCES, NM 88003

ROBERT NORTH  
CENTER FOR MONITORING RESEARCH  
1300 N. 17th STREET, SUITE 1450  
ARLINGTON, VA 22209

OFFICE OF THE SECRETARY OF DEFENSE  
DDR&E  
WASHINGTON DC 20330

JOHN ORCUTT  
INSTITUTE OF GEOPHYSICS AND PLANETARY PHYSICS  
UNIVERSITY OF CALIFORNIA, SAN DIEGO  
LA JOLLA, CA 92093

PACIFIC NORTHWEST NATIONAL LABORATORY  
ATTN: TECHNICAL STAFF (PLS ROUTE)  
PO BOX 999, MS K6-48  
RICHLAND, WA 99352

PACIFIC NORTHWEST NATIONAL LABORATORY  
ATTN: TECHNICAL STAFF (PLS ROUTE)  
PO BOX 999, MS K6-40  
RICHLAND, WA 99352

PACIFIC NORTHWEST NATIONAL LABORATORY  
ATTN: TECHNICAL STAFF (PLS ROUTE)  
PO BOX 999, MS K6-84  
RICHLAND, WA 99352

PACIFIC NORTHWEST NATIONAL LABORATORY  
ATTN: TECHNICAL STAFF (PLS ROUTE)  
PO BOX 999, MS K5-12  
RICHLAND, WA 99352

FRANK PILOTTE  
HQ AFTAC/TT  
1030 S. HIGHWAY A1A  
PATRICK AFB, FL 32925-3002

KEITH PRIESTLEY  
DEPARTMENT OF EARTH SCIENCES  
UNIVERSITY OF CAMBRIDGE  
MADINGLEY RISE, MADINGLEY ROAD  
CAMBRIDGE, CB3 OEZ UK

JAY PULLI  
BBN SYSTEMS AND TECHNOLOGIES, INC.  
1300 NORTH 17TH STREET  
ROSSLYN, VA 22209

DELAINE REITER  
SENCOM CORP.  
73 STANDISH ROAD  
WATERTOWN, MA 02172

PAUL RICHARDS  
COLUMBIA UNIVERSITY  
LAMONT-DOHERTY EARTH OBSERVATORY  
PALISADES, NY 10964

MICHAEL RITZWOLLER  
DEPARTMENT OF PHYSICS  
UNIVERSITY OF COLORADO  
CAMPUS BOX 390  
BOULDER, CO 80309-0309

DAVID RUSSELL  
HQ AFTAC/TTR  
1030 SOUTH HIGHWAY A1A  
PATRICK AFB, FL 32925-3002

CHANDAN SAIKIA  
WOODWARD-CLYDE FEDERAL SERVICES  
566 EL DORADO ST., SUITE 100  
PASADENA, CA 91101-2560

SANDIA NATIONAL LABORATORY  
ATTN: TECHNICAL STAFF (PLS ROUTE)  
DEPT. 5704  
MS 0979, PO BOX 5800  
ALBUQUERQUE, NM 87185-0979

SANDIA NATIONAL LABORATORY  
ATTN: TECHNICAL STAFF (PLS ROUTE)  
DEPT. 9311  
MS 1159, PO BOX 5800  
ALBUQUERQUE, NM 87185-1159

SANDIA NATIONAL LABORATORY  
ATTN: TECHNICAL STAFF (PLS ROUTE)  
DEPT. 5704  
MS 0655, PO BOX 5800  
ALBUQUERQUE, NM 87185-0655

SANDIA NATIONAL LABORATORY  
ATTN: TECHNICAL STAFF (PLS ROUTE)  
DEPT. 5736  
MS 0655, PO BOX 5800  
ALBUQUERQUE, NM 87185-0655

THOMAS SERENO JR.  
SCIENCE APPLICATIONS INTERNATIONAL  
CORPORATION  
10260 CAMPUS POINT DRIVE  
SAN DIEGO, CA 92121

AVI SHAPIRA  
SEISMOLOGY DIVISION  
THE INSTITUTE FOR PETROLEUM RESEARCH AND  
GEOPHYSICS  
P.O.B. 2286 NOLON 58122 ISRAEL

ROBERT SHUMWAY  
410 MRAK HALL  
DIVISION OF STATISTICS  
UNIVERSITY OF CALIFORNIA  
DAVIS, CA 95616-8671

DAVID SIMPSON  
IRIS  
1200 NEW YORK AVE., NW  
SUITE 800  
WASHINGTON DC 20005

JEFFRY STEVENS  
MAXWELL TECHNOLOGIES  
8888 BALBOA AVE.  
SAN DIEGO, CA 92123-1506

BRIAN SULLIVAN  
BOSTON COLLEGE  
INSITUTE FOR SPACE RESEARCH  
140 COMMONWEALTH AVENUE  
CHESTNUT HILL, MA 02167

TACTEC  
BATTELLE MEMORIAL INSTITUTE  
505 KING AVENUE  
COLUMBUS, OH 43201 (FINAL REPORT)

NAFI TOKSOZ  
EARTH RESOURCES LABORATORY, M.I.T.  
42 CARLTON STREET, E34-440  
CAMBRIDGE, MA 02142

LAWRENCE TURNBULL  
ACIS  
DCI/ACIS  
WASHINGTON DC 20505

GREG VAN DER VINK  
IRIS  
1200 NEW YORK AVE., NW  
SUITE 800  
WASHINGTON DC 20005

FRANK VERNON  
UNIVERSITY OF CALIFORNIA, SAN DIEGO  
SCRIPPS INSTITUTION OF OCEANOGRAPHY IGPP, 0225  
9500 GILMAN DRIVE  
LA JOLLA, CA 92093-0225

TERRY WALLACE  
UNIVERSITY OF ARIZONA  
DEPARTMENT OF GEOSCIENCES  
BUILDING #77  
TUCSON, AZ 85721

JILL WARREN  
LOS ALAMOS NATIONAL LABORATORY  
GROUP NIS-8  
P.O. BOX 1663  
LOS ALAMOS, NM 87545 (5 COPIES)

DANIEL WEILL  
NSF  
EAR-785  
4201 WILSON BLVD., ROOM 785  
ARLINGTON, VA 22230

RU SHAN WU  
UNIVERSITY OF CALIFORNIA SANTA CRUZ  
EARTH SCIENCES DEPT.  
1156 HIGH STREET  
SANTA CRUZ, CA 95064

JIAKANG XIE  
COLUMBIA UNIVERSITY  
LAMONT DOHERTY EARTH OBSERVATORY  
ROUTE 9W  
PALISADES, NY 10964

JAMES E. ZOLLWEG  
BOISE STATE UNIVERSITY  
GEOSCIENCES DEPT.  
1910 UNIVERSITY DRIVE  
BOISE, ID 83725